Supplement of Biogeosciences, 19, 3663–3682, 2022
https://doi.org/10.5194/bg-19-3663-2022-supplement

Biogeosciences Open Access EGU

Supplement of

Assessing the spatial and temporal variability of methylmercury biogeochemistry and bioaccumulation in the Mediterranean Sea with a coupled 3D model

Ginevra Rosati et al.

Correspondence to: Ginevra Rosati (grosati@ogs.it)

Content:

Table S1. Partition coefficients used in the modeling (Choe et al., 2003; Choe and Gill, 2003; Lamborg et al., 2016).

$K_{D\ Hg\text{-}POC}$	*Partition coefficient for HgII and POC*	l kg^{-1}	$1 \cdot 10^6$
$K_{D\ MMHg\text{-}POC}$	*Partition coefficient for MMHg and POC*	l kg^{-1}	$5 \cdot 10^5$
$K_{D\ Hg\text{-}DOC}$	*Partition coefficient for HgII and DOC*	l kg^{-1}	$2 \cdot 10^5$
$K_{D\ MMHg\text{-}DOC}$	*Partition coefficient for MMHg and DOC*	l kg^{-1}	$5 \cdot 10^5$

Table S2. Equations S1-S9, used in the model for the calculation of rate for Hg transformations (Zhang et al., 2020, Zhang et al., 2014).

Parameter		Units	Formula		Ref
k_{met}	*Hg^{II} methylation rate constant*	d^{-1}	$k_{met} = x_{met} \cdot remPOC$	*Eq. S1*	*1*
	MMHg methylation rate constant	d^{-1}	$k_{met2} = x_{met2}$	*Eq. S2*	*1*
k_{phdm}	*MMHg photo-demethylation rate constant*	d^{-1}	$k_{phdm} = x_{phdm} \cdot h\upsilon$	*Eq. S3*	*1*
k_{phdm2}	*DMHg photo-demethylation rate constant*	d^{-1}	$k_{phdm2} = x_{phdm2} + 3 \cdot 10^{-4} \cdot h\upsilon$	*Eq. S4*	*1*
k_{dem}	*MMHg dark demethylation rate constant*	d^{-1}	$k_{dem} = 9.5 \cdot 10^{-4} + exp(-5500 \cdot (\frac{1}{T} - \frac{1}{293.15}))$	*Eq. S5*	*1*
k_{phox}	*Hg^0 photoxidation rate constant*	d^{-1}	$k_{phox} = x_{phox} \cdot h\upsilon$	*Eq. S6*	*2*
k_{phr}	*Hg^{II} photoreduction rate constant*	d^{-1}	$k_{phr} = x_{phr} \cdot h\upsilon$	*Eq. S7*	*2*
k_{biox}	*Hg^0 biotic oxidation rate constant*	d^{-1}	$k_{biox} = 0.138 \cdot remPOC$	*Eq. S8*	*2*
k_{biored}	*Hg^{II} biotic reduction rate constant*	d^{-1}	$k_{bred} = 0.086 \cdot remPOC$	*Eq. S9*	*2*
x_{met}	*Coefficient for Hg methylation*	m^3 mmol^{-1}	0.038		*1*
x_{met2}	*Coefficient for MMHg methylation*	d^{-1}	0.0008		*1*
x_{phdm}	*Coefficient for MMHg photo-demethylation*	m^2 W^{-1} d^{-1}	0.007		*1*
x_{phdm2}	*Coefficient for DMHg photo-demethylation*	m^2 W^{-1} d^{-1}	0.02		*1*
x_{phox}	*Coefficient for biotic oxidation*	m^3 mmol^{-1}	0.56		*2*
x_{phr}	*Coefficient for biotic reduction*	m^3 mmol^{-1}	0.14		*2*
remPOC	*POC remineralization*	mmol m^{-3} d^{-1}	BFM model output		
$h\upsilon$	*Shortwave radiation flux*	W m^{-2}	BFM model output		
1. Zhang et al., 2020 2. Zhang et al., 2014					

Table S3. Phytoplankton functional types (PFTs) of the BFM model with estimated cell-size parameters (radius, surface area, volume, and R_{SV}).

PFT	Functional group	Radius (µm)	Surface	Volume	R_{SV}
P1	*Diatoms*	55	38,013.24	696,909.38	0.05
P2	*Aut. nanoflagellates*	5.5	380.13	696.91	0.55
P3	*Picoplankton*	0.55	3.80	0.70	5.45
P4	*Large phytoplankton*	150	282,743.10	14,137,155.00	0.02

Table S4. Conversion factors used to convert carbon variables of plankton pfts to Wet Weight, derived from published experimental data (Jørgensen et al., 1979).

	Carbon as % of Dry Weight	Dry Weight /Wet Weight Ratio	Carbon/Wet Weight ratio	Applied to pft
Diatoms	37.5	0.31	8.6002	P1
Cyanobacteria	46.69	0.563	3.0842	P3
Chlorophyceae	42.5	0.4705	5.0009	P2
Dinoflagellata	NA *	0.341	7.8201	P4
Carnivorous mesozooplankton	44	11.6	19.6	Z3-Z6
	** used diatoms conversion factor*			

Table S5. Summary of information used to set initial conditions for Hg species in the Mediterranean Sea (Horvat et al. 2003; Cossa and Coquery 2005; Kotnik et al. 2007, 2015; Cossa et al. 2017).

ALB				**SWM**			
Hg_T	*average profile from figure*	*August 2003*	*1*	**Hg_T**	*average profile from figure*	*August 2003 March/April 2004*	*1, 2*
MeHg	*average profile from figure*	*August 2003*	*1*	**MeHg**	*average profile from figure*	*August 2003 March/April 2004*	*1*
DMHg	*from estimated DMHg:DGM ratio in NWM*	-	*2*	**DMHg**	*from estimated DMHg:DGM ratio in NWM*	-	*2*
DGM	*average profile from figure*	*August 2003*	*1*	**DGM**	*average profile from figure*	*August 2003 March/April 2004*	*1*
Hg^0	*by difference (DGM-DMHg)*	-	-	**Hg^0**	*by difference (DGM-MHg)*	-	-
Hg^{II}	*by difference (HgT-MMHg-DMHg-Hg0)*	-	-	**Hg^{II}**	*by difference (HgT-MMHg-DMHg-Hg0)*	-	-
NWM				**CWM**			

Hg_T	*average profile from figure*	*August 2000 March/April 2004*	*2*	**Hg_T**	*st. 19 profile from table*	*Jul/Aug 2000*	*4*
MeHg	*average profile from figure*	*May 2006*	*3*	**MeHg**	*st. 19 profile from table*	*Jul/Aug 2000*	*4*
DMHg	*average profile from figure*	*August 2000 March/April 2004*	*2*	**DMHg**	*st. 19 profile from table*	*Jul/Aug 2000*	*4*
DGM	*average profile from figure*	*August 2000*	*1*	**DGM**	*st.19 profile from figure*	*Jul/Aug 2000*	*5*
Hg^0	*by difference (DGM-DMHg)*	-	-	**Hg^0**	*by difference (DGM-DMHg)*	-	-
Hg^{II}	*by difference (HgT-MMHg-DMHg-Hg0)*	-	-	**Hg^{II}**	*by difference (HgT-MMHg-DMHg-Hg0)*	-	-
TYR				**SIC**			
Hg_T	*average profile from figure*	*August 2000 March/April 2004*	*1, 2*	**Hg_T**	*average profile from figure*	*March/April 2004*	*1*
MeHg	*average profile from figure*	*August 2003 March/April 2004*	*1*	**MeHg**	*average profile from figure*	*March/April 2004*	*1*
DMHg	*estimated based on DMHg:DGM ratio in NWM*		-	**DMHg**	*estimated based on DMHg:DGM ratio in NWM*		-
DGM	*average profile from figure*	*August 2003 March/April 2004*	*1*	**DGM**	*average profile from figure*	*March/April 2004*	*1*
Hg^0	*by difference (DGM-DMHg)*	-	-	**Hg^0**	*by difference (DGM-DMHg)*	-	-
Hg^{II}	*by difference (HgT-MMHg-DMHg-Hg0)*	-	-	**Hg^{II}**	*by difference (HgT-MMHg-DMHg-Hg0)*	-	-
ION				**LEV**			
Hg_T	*average profile from figure*	*August 2003*	*1*	**Hg_T**	*from ION profile*	*August 2003*	*1*
MeHg	*average profile from figure*	*August 2003*	*1*	**MeHg**	*average profile from figure*	*August 2003*	*1*
DMHg	*estimated based on DMHg:DGM ration in NWM*	-	-	**DMHg**	*estimated based on DMHg:DGM ratios in NWM*	-	-
DGM	*average profile from figure*	*August 2003*	*1*	**DGM**	*average profile from figure*	*August 2003*	*1*
Hg^0	-	-		**Hg_T**	-	-	-
Hg^{II}	-	-		**MeHg**	-	-	-
NAD				**SAD**			
HgT	*average profile from stations in Table S1 and S2*	*October/November 2004 June 2005*	*6*	**DGM**	*average profile from stations in Table S1 and S2*	*October/November 2004 June 2005*	*6*

MMHg	*average profile from Table S1 and S2*	*October/November 2004 June 2005*	*6*	**Hg^0**	*average profile from stations in Table S1 and S2*	*October/November 2004 June 2005*	*6*
DMHg	*average profile from Table S1 and S2*	*October/November 2004 June 2005*	*6*	**Hg^{II}**	*average profile from Table S1 and S2*	*October/November 2004 June 2005*	*6*
DGM	*average profile from Table S1 and S2*	*October/November 2004 June 2005*	*6*	**DGM**	*average profile from Table S1 and S2*	*October/November 2004 June 2005*	*6*
	1. Kotnik et al 2007; 2. Cossa e& Coquery 2005; 3. Cossa et al 2017; 4. Horvat et al 2003; 5. Ferrara e al 2003; 6. Kotnik et al 2015						

Table S6. Concentrations of riverine Hg_T and MMHg used in the model setup, and resulting annual load

River Name	Hg_T	MMHg	Hg_T	MMHg	Notes and References
	pM	pM	Mg y^{-1}	Mg y^{-1}	
Grand Rhone	53	1.06	0.62	0.0355	*HgP = 0.85 nmol/g* [1] *SPM = 60 mg/l* [2]
Petit Rhone	53	1.06	0.07	0.0039	
Soca/sonzo	170	1.02	0.23	0.0294	*90-249 pM at the river mouth* [3]
Ebro	102	2.04	0.23	0.0070	*HgP = 4.98 nmol/g* [4] *SPM = 20 mg/l* [4]
Po Maistra	120	2.4	0.06	0.0030	*HgP = 1.15 nmol/g* [5] *SPM = 30 mg/l* [5]
Po Tramontana	120	2.4	0.14	0.0071	
Po Dritta	120	2.4	0.39	0.0201	
Po Scirocco + Po Bonifazi	120	2.4	0.12	0.0062	
Po Bastimento	120	2.4	0.05	0.0028	
Po Bocca Tolle	120	2.4	0.20	0.0102	
Po Gnocca	120	2.4	0.21	0.0106	
Po Goro	120	2.4	0.13	0.0067	
Po Levante	120	2.4	0.02	0.0010	
Po Volano	120	2.4	0.01	0.0003	
Nile	120	2.4	0.28	0.0074	*Impacted by Artisanal Small-Scale Gold Mining* [6]
Nile	120	2.4	0.28	0.0074	
Tevere/Tiber	100	2	0.07	0.0136	*High mineral Hg content in soils* [7]
Tevere/Tiber	100	2	0.07	0.0136	
Reno	80	1.6	0.03	0.0012	*Impacted by Industries and Agriculture* [7]
Vjiose	53	1.06	0.04	0.0026	

Seman	53	1.06	0.02	0.0012
Buna/Bojana	53	1.06	0.10	0.0060
Buna/Bojana	53	1.06	0.10	0.0060
Piave	53	1.06	0.05	0.0030
Tagliamento	53	1.06	0.03	0.0018
Livenza	53	1.06	0.04	0.0023
Brenta-Bacchiglione	53	1.06	0.07	0.0038
Adige	53	1.06	0.08	0.0049
Lika	53	1.06	0.02	0.0014
Krka	53	1.06	0.02	0.0010
Arno	53	1.06	0.03	0.0017
Neretva	53	1.06	0.07	0.0043
Aude	53	1.06	0.03	0.0015
Trebisjnica	53	1.06	0.03	0.0017
Mati	53	1.06	0.03	0.0018
Volturno	53	1.06	0.02	0.0009
Shkumbini	53	1.06	0.02	0.0010
Struma/Strymonas	53	1.06	0.02	0.0014
Meric/Evros/Maritsa	53	1.06	0.05	0.0028
Axios/Vardar	53	1.06	0.03	0.0016
Arachtos	53	1.06	0.02	0.0014
Pinios	53	1.06	0.02	0.0011
Acheloos	53	1.06	0.03	0.0019
Gediz	53	1.06	0.02	0.0012
Buyuk Menderes	53	1.06	0.04	0.0024
Kopru	53	1.06	0.04	0.0022
Manavagat	53	1.06	0.06	0.0032
Seyhan	53	1.06	0.07	0.0038
Ceyhan	53	1.06	0.07	0.0042
Goksu	53	1.06	0.09	0.0051
Medjerda	53	1.06	0.03	0.0017
Asi/Orontes	53	1.06	0.03	0.0015
Total Load (Mg y^{-1})			4.62	0.27

(1) Cossa et al., 2017; (2) Bourgeois et al., 2011; (3) Hines et al., 2000; (4) Palanques et al., 2020; (5) Vignati et al., 2003; (6) Ahmed et al., 2018; (7) Panagos et al., 2021

Equation S10. Parameterization for Hg methylation tested in model sensitivity analysis as alternative to equation S1.

$$k_{met} = x_{met} \cdot (remPOC + remDOC) \qquad \textit{Eq. S10}$$

Supplemental Section 1. Results of the sensitivity analyses

Supplemental Section S1.1. Sensitivity to POC sinking velocity

The sensitiviy analysis highlighted that the sinking velocity (w_s) of organic detritus (POC) has a strong impact of on the vertical profiles of MeHg (MMHg+DMHg), by controlling the vertical distribution of POC concentrations and, consequently, of POC remineralization rates (Fig. S1). The changes in bacterial activity driven by the different distribution of POC in the water column also prompt higher net biological reduction the intermediate waters resulting in a slight increase of Hg^0 (Fig. S1.2). The POC sinking velocity affect the sinking velocity of particulate Hg species (Hg^{II}_P and $MeHg_P$), however the small differences among vertical profiles of Hg^{II} (Fig. S1) and Hg_T (Fig. S2) indicate that this process has a limited impact, likely due to the small fraction represented by particulate Hg species (<1%-2%) in the open sea, where particle concentrations are low (~0.02 mg/l). The hypothesis of POC sinking velocity influencing the vertical distribution of Hg species was thus confirmed, with a stronger effect on MMHg than on inorganic Hg (Fig. S1). The hypotesys of an increase in modeled MeHg concentrations at higher sinking velocity, driven by a deepening of the net Hg methylation limiting the photochemical degradation of MeHg was instead disproven, as modeled maxima of MeHg concentrations are ~0.15 pM for all the three sensitivity simulations (Figure S1.1), which is far from the observed MeHg maxima (>0.4 pM) from various cruises in the Mediterranean Sea (Cossa et al., 2009). These, as well as other (e.g. Cossa et al., 2018; Heimbürger et al., 2010), field observations show that the peaks of MeHg profiles were located between ~250 and ~500 m-depth at most of Mediterranean deep stations, which is best reproduced (Fig. S1 and 5) in the simulation adopting w_s = 10 m d^{-1}, which is the same value used in the global coupled biogeochemical Hg model (Ward et al., 2012; Zhang et al., 2020).

The choice to retain the simulation with w_s = 10 m d^{-1} is also supported by a comparison between the modeled POC fluxes at 200 m depth and the observational dataset compiled by Ramondenc et al., (2016). The simulation with w_s = 20 m d^{-1} was excluded a priori as it leaded to an excessive reduction of organic carbon in surface waters (Fig. S1) and did not improve model performance with regard to MeHg dynamics. The simulation with w_s = 10 m d^{-1} improved the model ability to reproduce the spring fluxes at all subbasins analyzed with respect to the simulation with w_s = 3 m d^{-1} (Fig. S3). The impact of sinking velocity on winter fluxes is very limited, while in the other seasons there are contrasting results depending on the subbasin (Fig. S3). In autumn, the agreement with observations for the simulation with w_s = 10 m d^{-1} improves for the in the *Nwm* and *Ion* subbasins but decreases for the *Lev4* subbasin. Conversely, during summer, the simulation with w_s = 10 m d^{-1} leads to an overestimation of fluxes in the *Nwm* and *Ion* subbasins and to an improvement of fluxes in the *Lev4*.

Overall, the simulation with w_s = 3 m d^{-1} has a higher RMSE (14.7) than the simulation with w_s = 10 m d^{-1} (RMSE=11.6).

Supplemental Section S1.2 Sensitivity to Hg methylation rate constant

The model sensitivity to different parameterizations of Hg methylation is shown in Fig. S1.4. The inclusion of the DOC remineralization in the equation for Hg methylation (Eq. S10), led to a MeHg increase only in surface waters that is not supported by the observations. On the other hand, a threefold increase in the Hg methylation constant x_{met} causes an increase in MeHg concentrations at the depths where maxima in MeHg concentrations have been observed (Cossa et al., 2022; 2009).

Supplemental Section S1.3. Sensitivity to Hg river loadings

The sensitivity analysis on Hg input from rivers was performed by implementing two simulations aimed at being representative of the lower (0.28 Mg y^{-1}) and upper bound (4.6 Mg y^{-1}) of river loadings (Sect. 2.3.3 in the main text). The load of organic particles from rivers, previously not included in the model setup, was added to account for the effects of coastal sedimentation, assuming an average concentration of 5 mg l^{-1} for all the rivers (Burgeois et al., 2011). This attempt to include costal dynamics is still a first approximation for several reasons including the limited spatial and temporal coverage of data to validate coastal processes (Cossarini et al., 2021; Liu et al., 2021) and the absence in this model of a tracer for inorganic solids load.

The comparison between the modeled POC fluxes at 200 m depth and the observational dataset compiled by Ramondenc et al., (2016) performed to validate the test on sinking velocity (Supplemental Sect. 1.1) was repeated for the simulation including riverine POC sources against the refence simulation, showing very limited to no changes in the fluxes in the open waters (Fig. S5).

The results showed little sensitivity of the Hg state variables in the open waters to the prescribed variation in river loadings, as the impacts are mostly limited to coastal areas in the nearby of major rivers (Fig. S6). The highest impacts are in surface waters (0-500 m depth) (Figs. S7-S9) and variations minimum at greater depths (e.g., Fig. S10). In the western subbasins, the variation of Hg species and Hg_T concentrations in surface waters (Figure S7) is mostly in the range 1-2%, except for an increase of 3-7% in the most surficial layers (0-100 m) of the *Nwm* influenced by the high discharge of the Rhône River. In the eastern subbasins, there is more variability in response (Figs. S8-S10): the highest increases are in the coastal subbasin *Nad* (about 20% for Hg_T and >25% for MMHg) that receive high Hg loadings from the Po and Soca/Isonzo Rivers, also affecting the southernmost confining subbasin *Sad* (with variation of 10-20% for Hg_T and about 10% for MMHg in the upper 100 m). The easternmost and shallowest part of the Levantine Sea (*Lev4)* also shows relatively high

variations (4-7% for Hg_T and MMHg in the first 100 m), while the impacts are lower (1-4%) in the other subbasins. Overall, these results imply small variation in modelled concentrations, and it should be noted that excluding the shallow *Nad* subbasins, the variations in MMHg concentrations are maxima at the top of the water column where concentrations are very low (<0.02-0.06 pM).

Figure S1. Sensitivity to POC sinking velocity (w_s) of modeled profiles of HgII concentrations, MeHg concentrations, and POC remineralization flux and concentrations (Supplemental Sect. S1.1). The output shown are mediated for August 2017 for the *Sad* (upper panels), *Nwm* (central panels), and *Lev* (bottom panels) subbasins, for the simulations with w_s = 3 m d^{-1} (blue lines), w_s= 10 m d^{-1} (green lines), and w_s= 20 m d^{-1} (yellow lines).

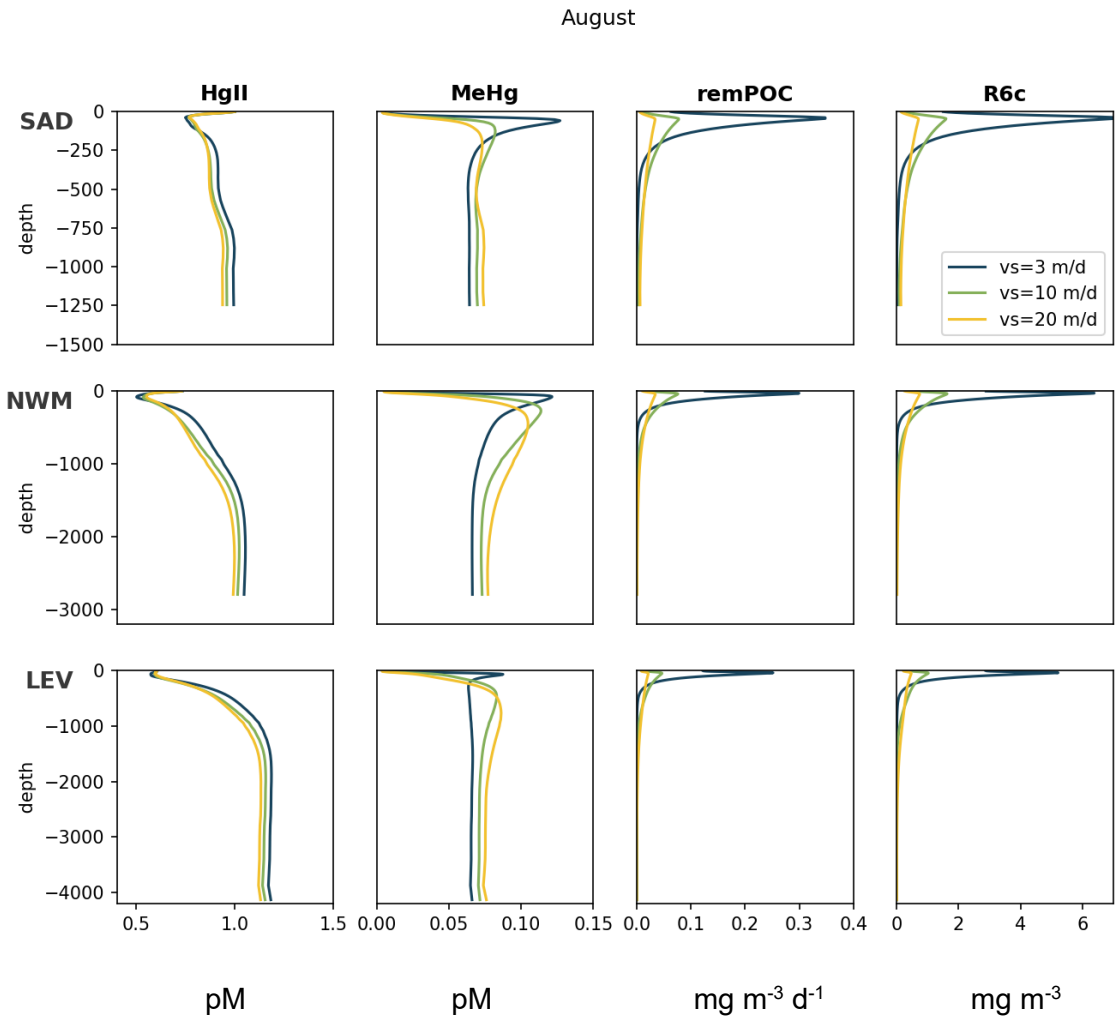

Figure S2. Sensitivity to POC sinking velocity (w_s) of modeled profiles of HgT, Hg^0, MMHg, and DMHg concentrations (Supplemental Sect. S1.1). The output shown are mediated for August 2017 for the *Sad* (upper panels), *Nwm* (central panels), and *Lev* (bottom panels) subbasins, for the simulations with w_s = 3 m d^{-1} (blue lines), w_s= 10 m d^{-1} (green lines), and w_s= 20 m d^{-1} (yellow lines).

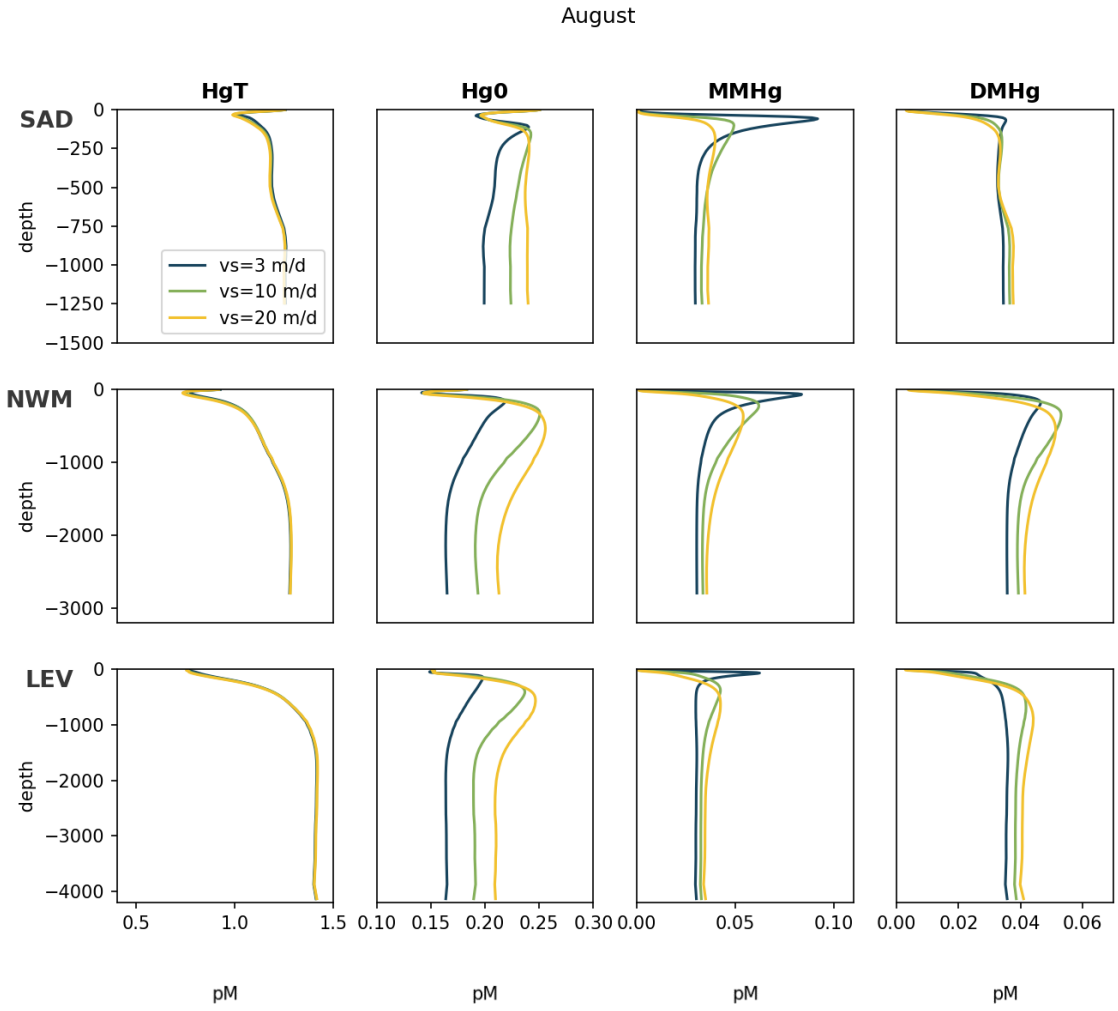

Figure S3. Seasonal dynamics of Particulate Organic Carbon fluxes in various subbasins of the Mediterranean Sea. The fluxes (mg m^{-2} d^{-1}) calculated from monthly mean model output are shown for the two simulations (Supplemental Sect. S1.1) assuming w_s = 3 m d^{-1} (dashed blue line for the average and shaded area for minimum and maximum values) and w_s =10 m d^{-1} (solid black line and grey shaded area), compared with observations (red dots and bars indicate the seasonal median and the I and III quartiles) compiled by Ramondenc et al., (2016).

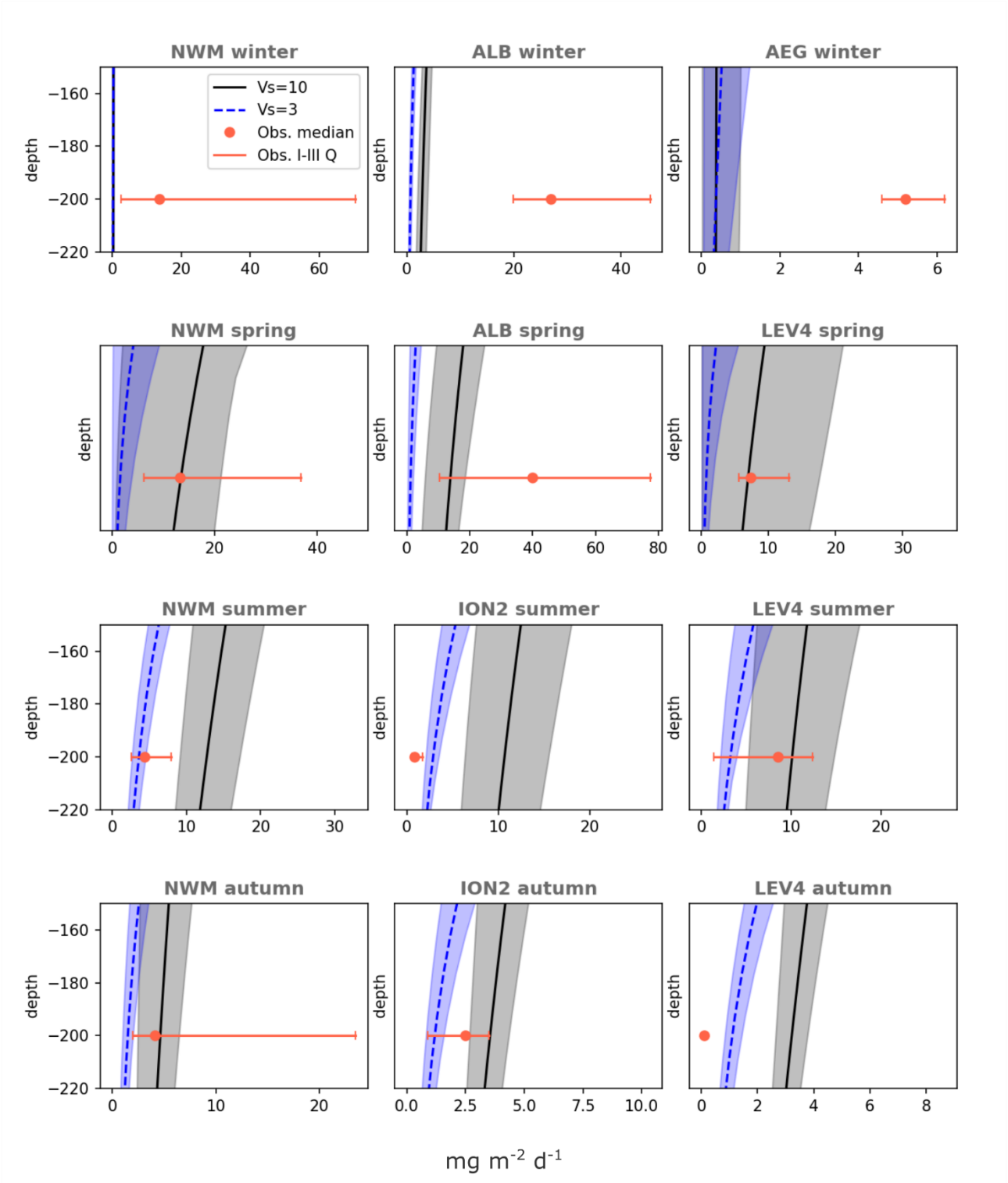

Figure S4. Sensitivity of modeled MeHg concentrations (pM) to different parameterization of Hg methylation (Supplemental Sect. S1.2): 1) x_{met} coefficient from the global model (green lines) as given in Table S1, 2) parameterization that include both POC and DOC remineralization (blue lines) as given in Eq. S10, and 3) threefold increase of the coefficient fot Hg methylation x_{met} (yellow lines). The output shown are mediated for May, June, July, and August 2017 for the subbasins *Sad* (upper panels), *Nwm* (central panels), and *Lev* (bottom panels).

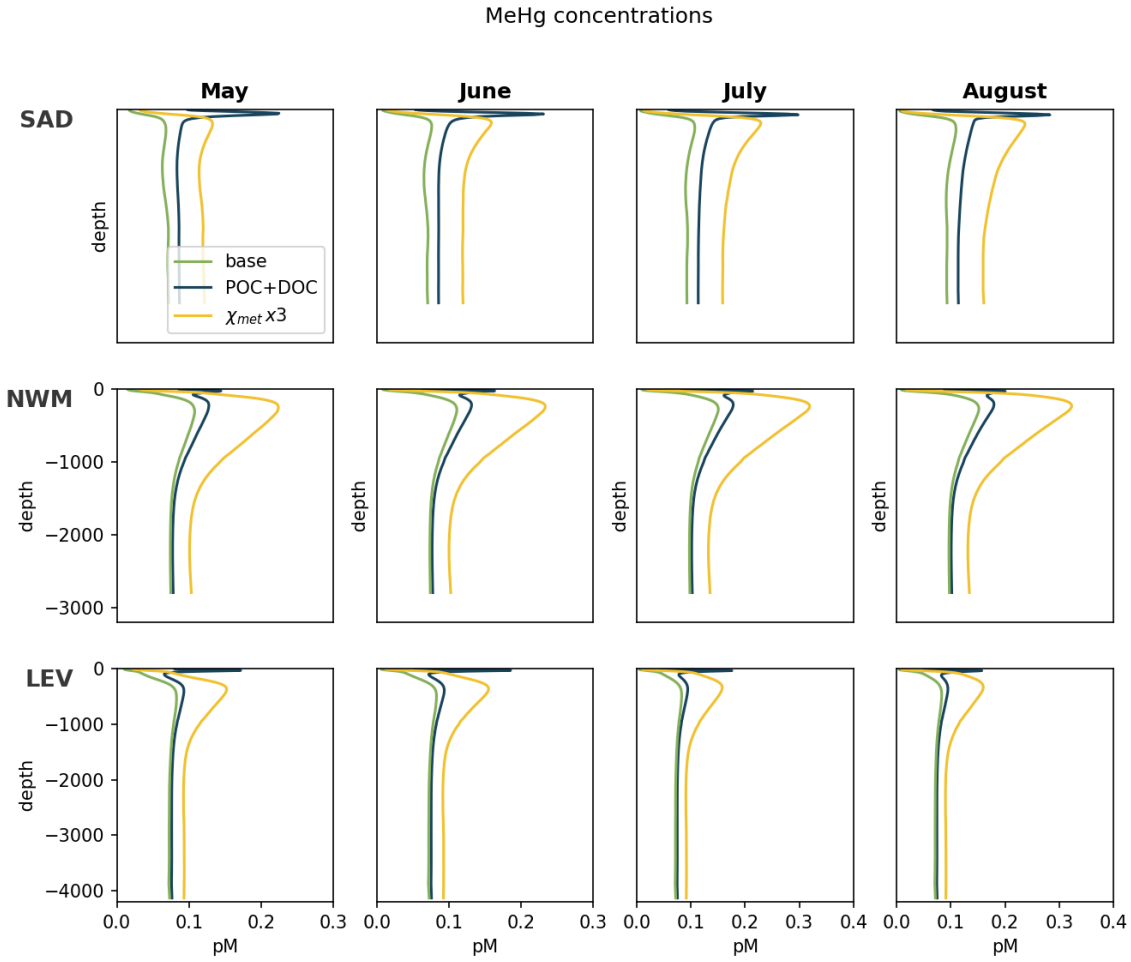

Figure S5. Seasonal dynamics of Particulate Organic Carbon fluxes in various subbasins of the Mediterranean Sea. The fluxes (mg m^{-2} d^{-1}) calculated from monthly mean model output are shown for the simulation with POC input from rivers (dashed blue line for the average and shaded area for minimum and maximum values) and for the reference simulation including only dissolved river inputs (solid black line and grey shaded area) (Supplemental Sect. S1.3), compared with observations (red dots and bars indicate the seasonal median and the I and III quartiles) compiled by Ramondenc et al., (2016).

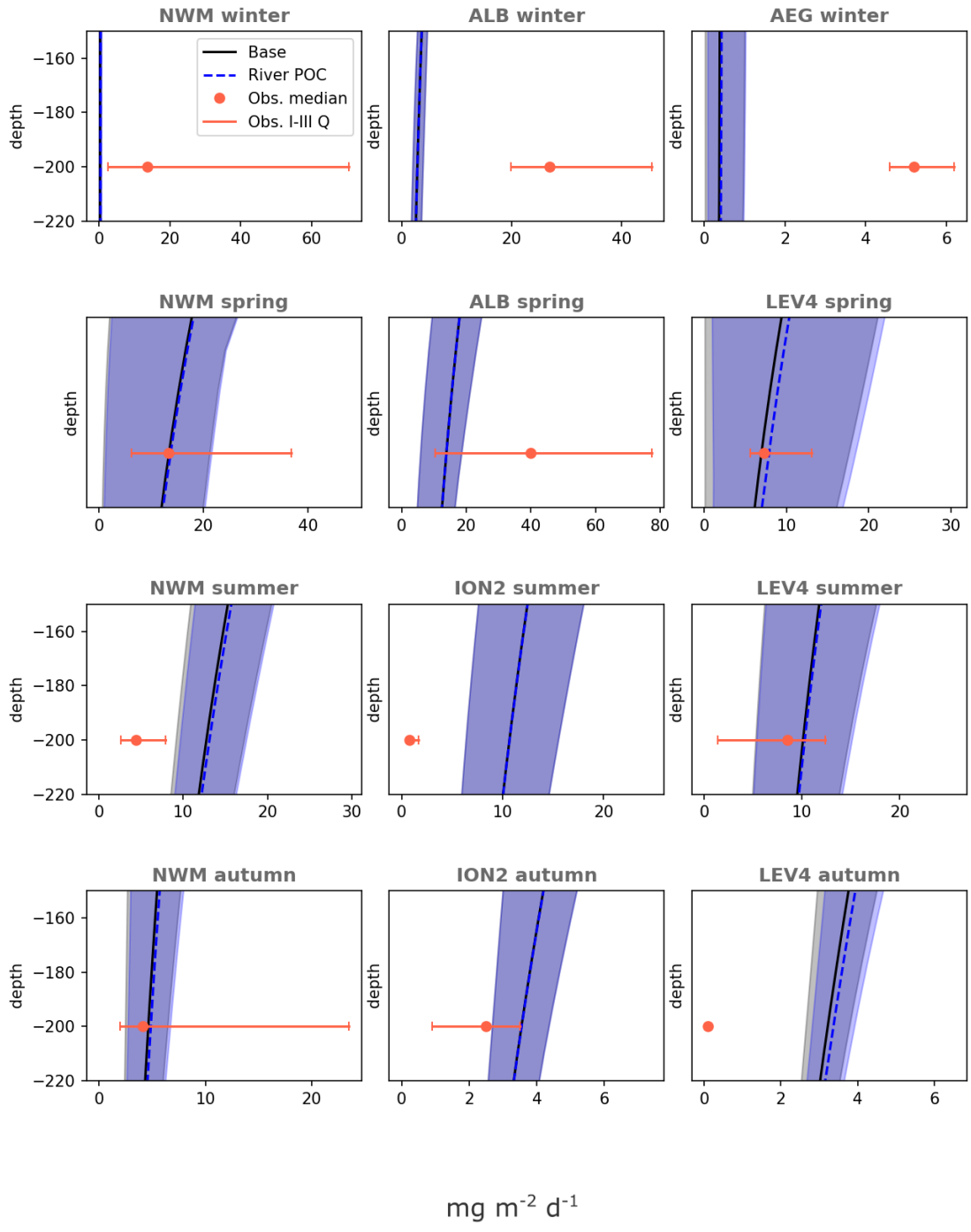

Figure S6. Spatial distribution of the variation (%) in modelled concentration of Hg^{II} for the simulation including input of particulate Hg from river (Supplemental Sect. S1.3) at different depths (25 m, 60 m, and 100 m) and months (January, April, July, and October).

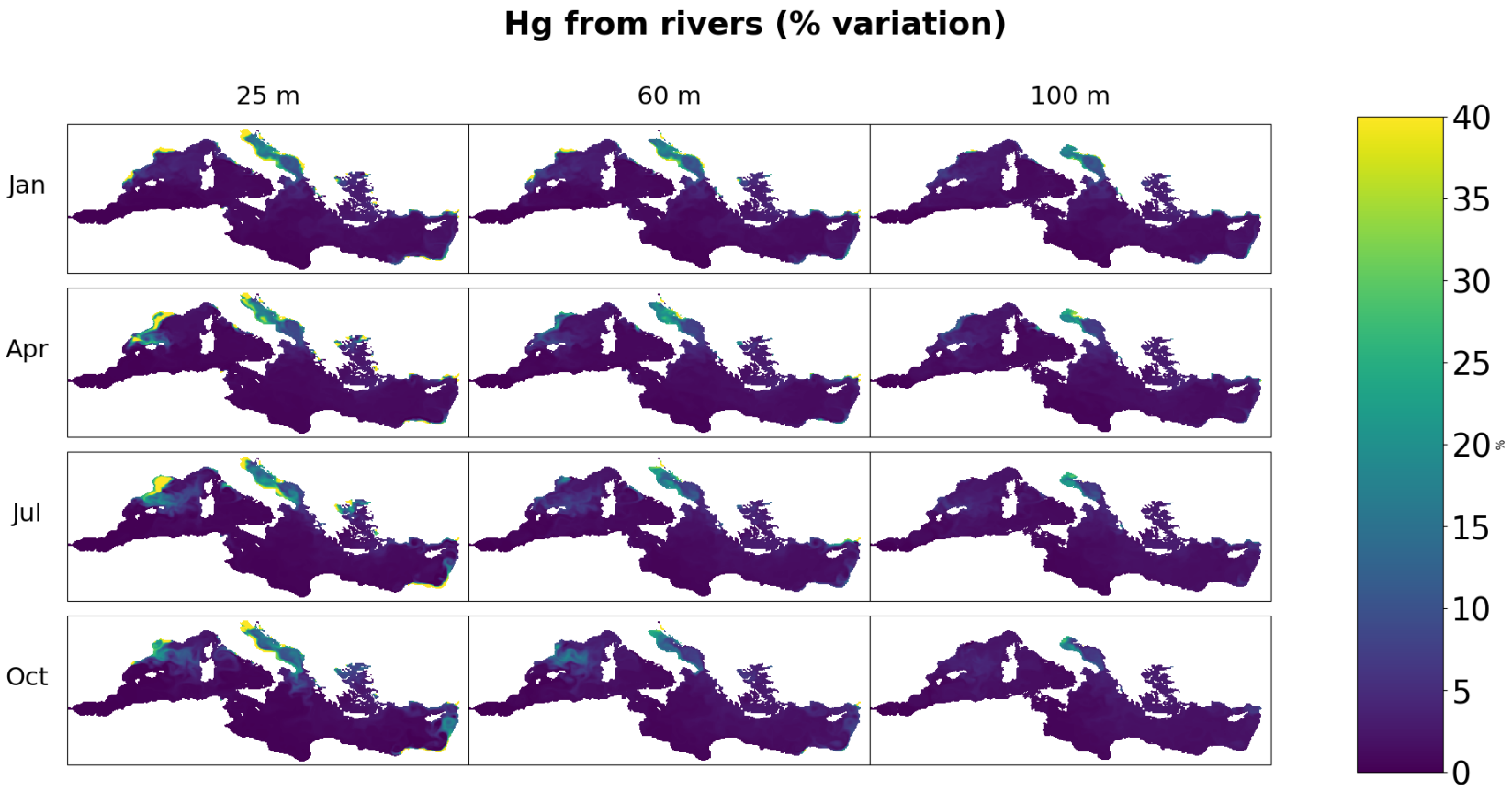

Figure S7. Impact of the simulation with high riverine Hg loads (Supplemental Sect. S1.3) on the seasonal average concentration profiles in surface waters (0-500 m depth) of different subbasins of the Western Mediterranean Sea (*Alb, Nwm, Swm, and Tyr*). The % variation with respect to the reference simulation is shown for each Hg species (Hg^{II}: yellow dashed line, Hg^0: dotted cyan line, MMHg: dash-dotted purple line, DMHg: dotted violet line).

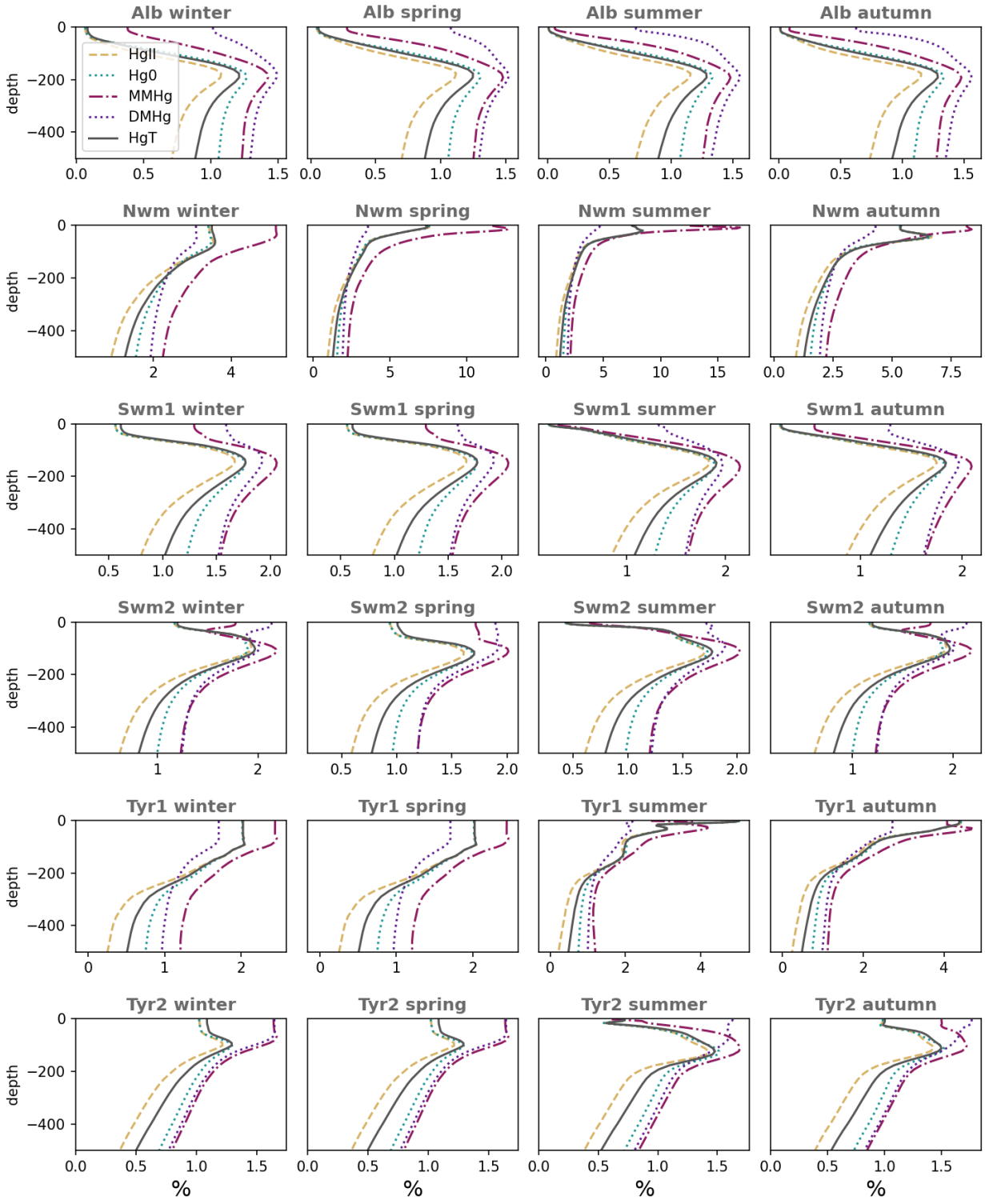

Figure S8. Impact of the simulation with high riverine Hg loads (Supplemental Sect. S1.3) on the seasonal average concentration profiles in surface waters (0-500 m depth) of different subbasins of the Eastern Mediterranean Sea (*Nad, Sad, Aeg, and Lev*). The % variation with respect to the reference simulation is shown for each Hg species (Hg^{II}: yellow dashed line, Hg^{0}: dotted cyan line, MMHg: dash-dotted purple line, DMHg: dotted violet line).

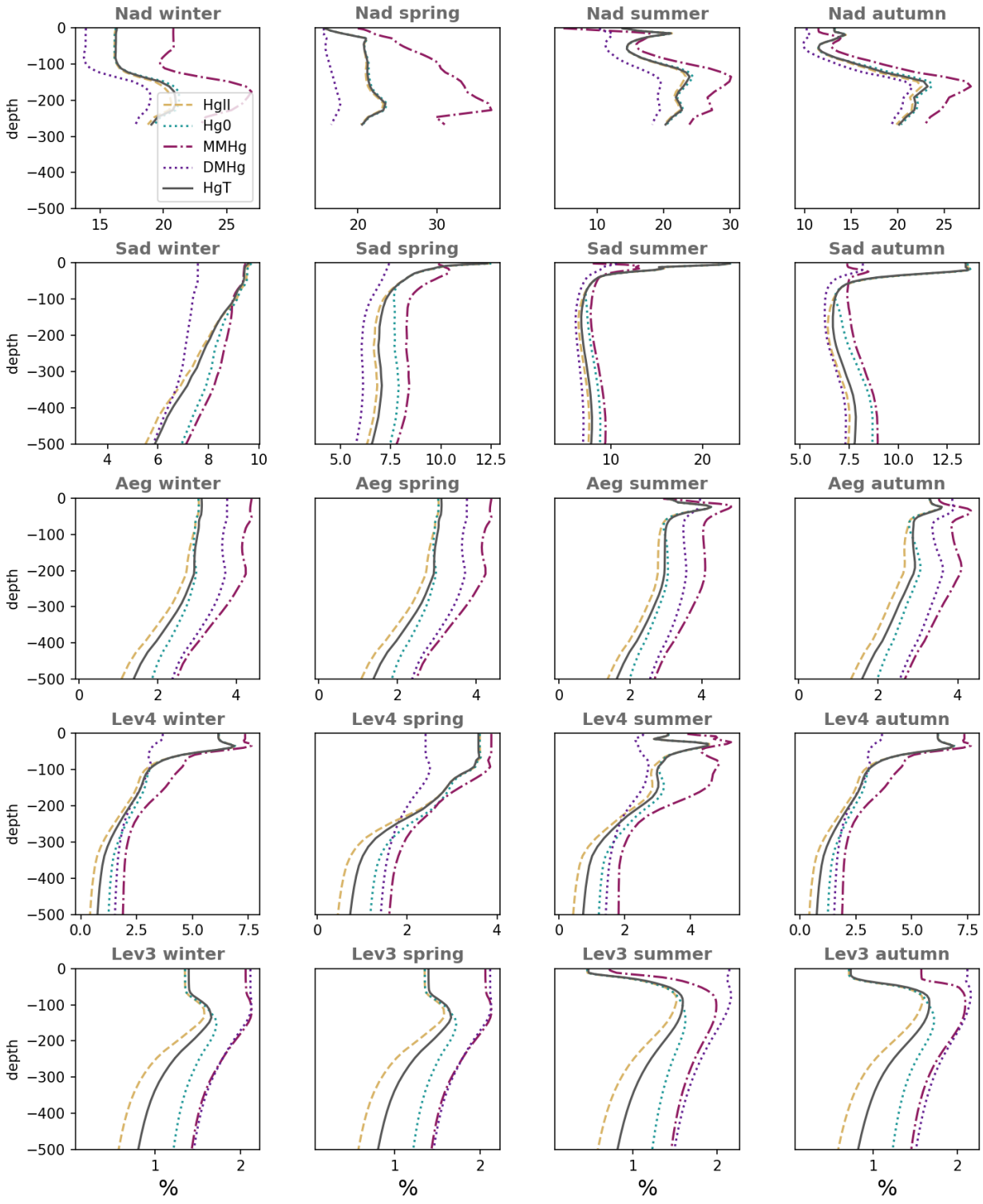

Figure S9. Impact of the simulation with high riverine Hg loads (Supplemental Sect. S1.3) on the seasonal average concentration profiles in surface waters (0-500 m depth) of different subbasins of the Eastern Mediterranean Sea (*Ion and Lev*). The % variation with respect to the reference simulation is shown for each Hg species (Hg^{II}: yellow dashed line, Hg^{0}: dotted cyan line, MMHg: dash-dotted purple line, DMHg: dotted violet line).

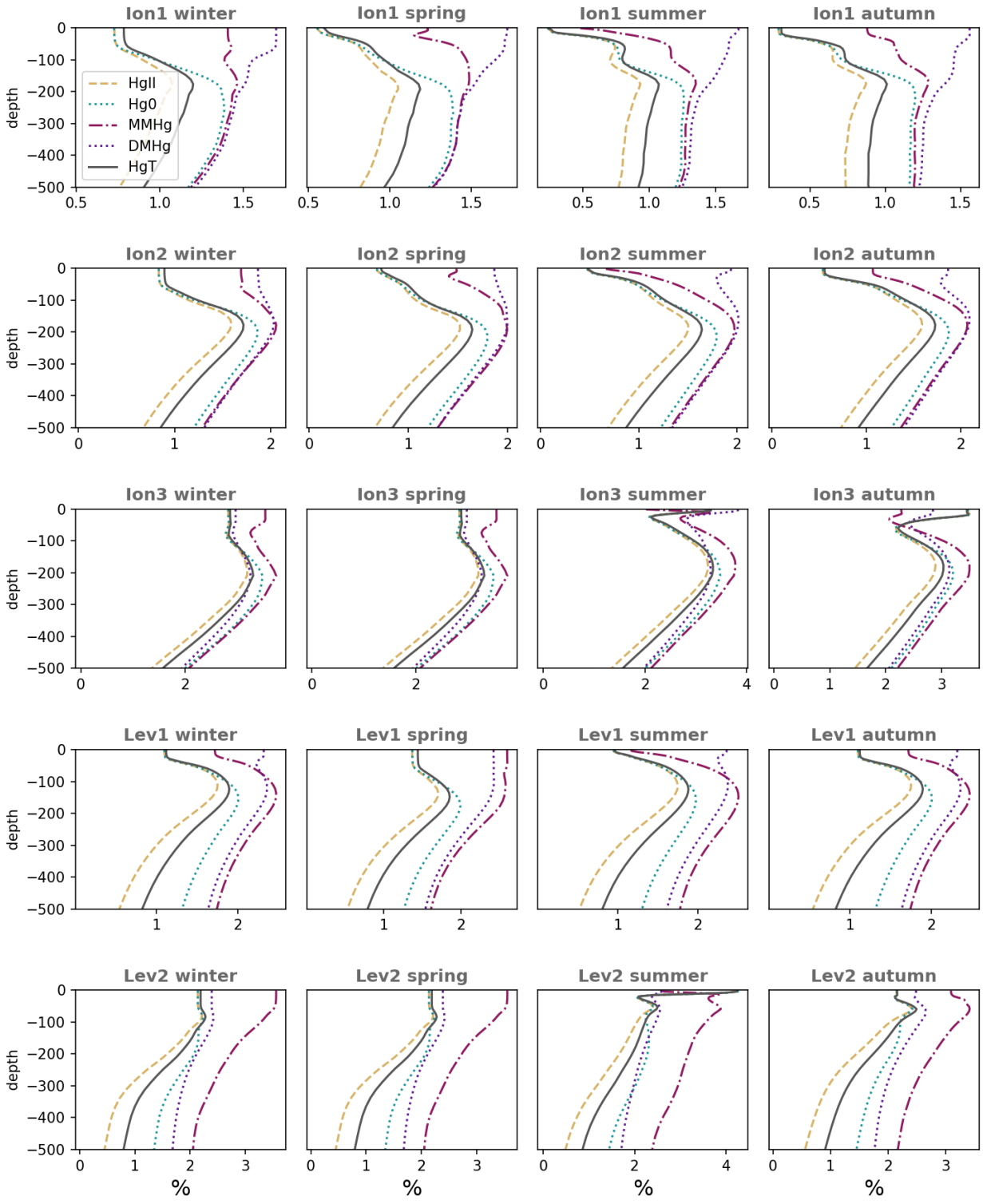

Figure S10. Impact of the simulation with high riverine Hg loads (Supplemental Sect. S1.3) on the seasonal average concentration profiles in the water column of different subbasins of the Eastern Mediterranean Sea (*Ion and Lev*). The % variation with respect to the reference simulation is shown for each Hg species (Hg^{II}: yellow dashed line, Hg^0: dotted cyan line, MMHg: dash-dotted purple line, DMHg: dotted violet line).

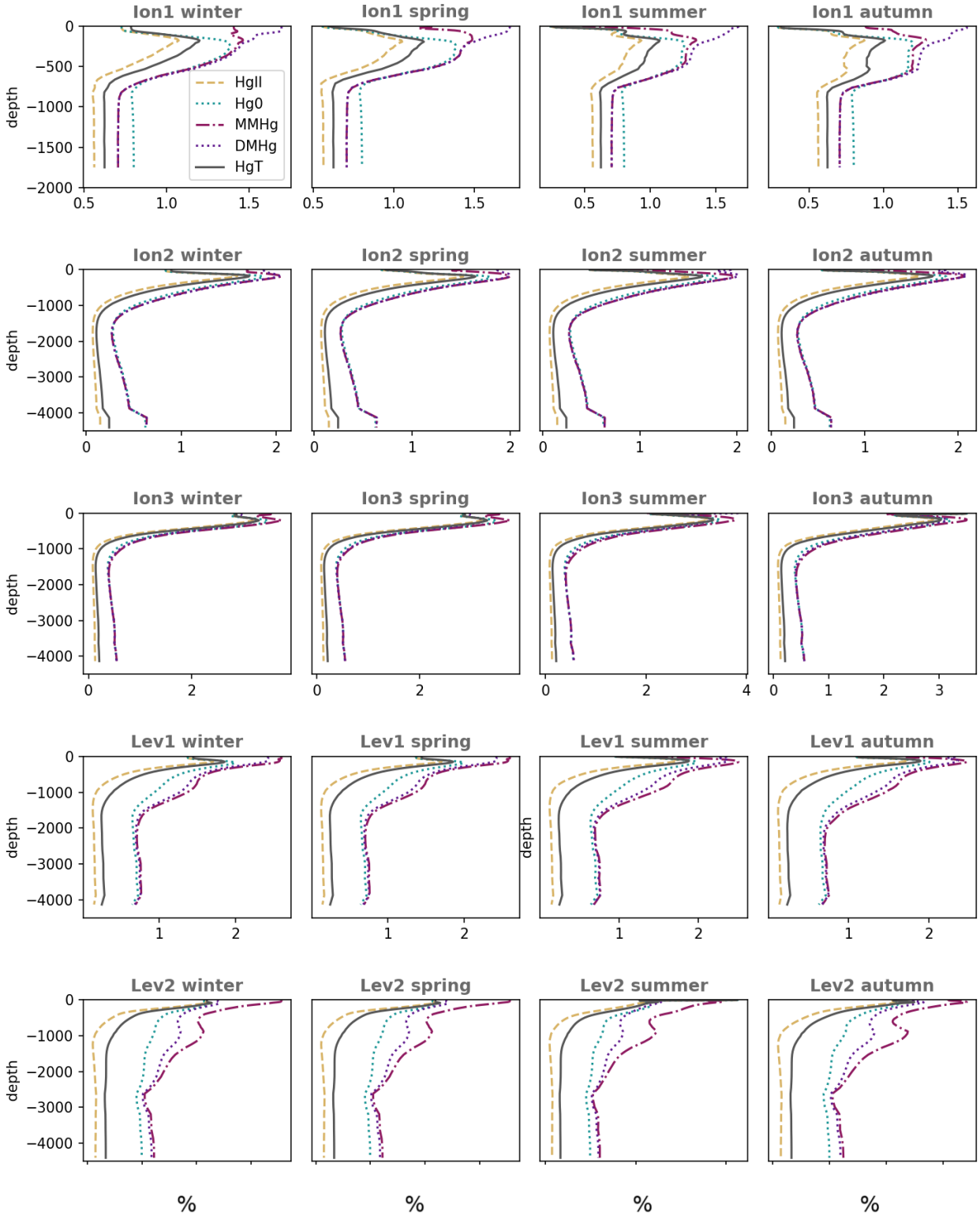

Figure S11. Comparison between monthly averaged modeled Hg_T concentrations (pM) profiles for 2017, after 13 years of model spin-up, and experimental observations from the literature that were used to constrain model initial conditions (Table S5). The observations are from Cossa et al., (2009) (*) and Kotnik et al., (2015) (^).

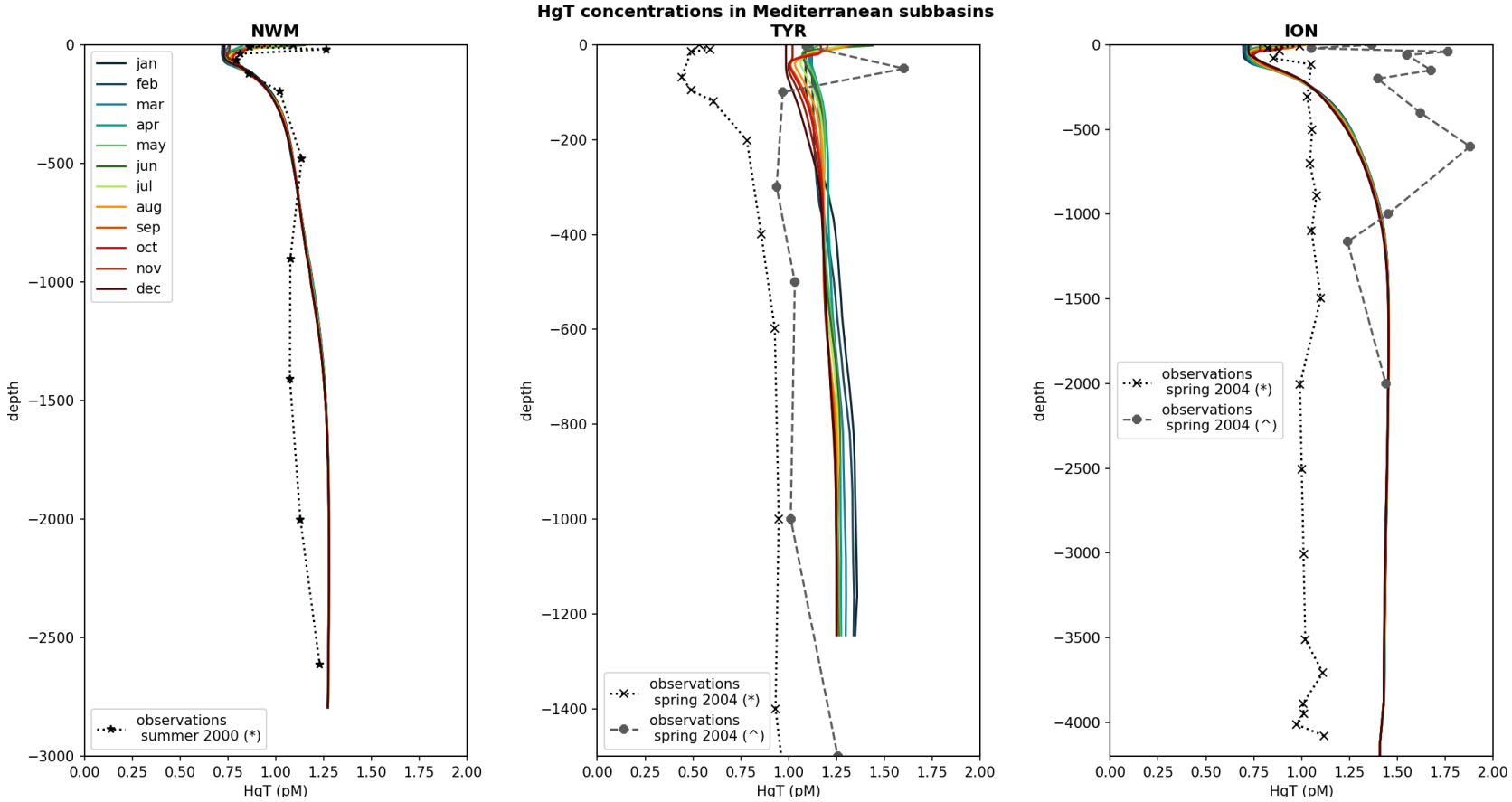

Figure S12. Monthly evolution of modeled reactions rate constants (d^{-1}) for photodemethylation (k_{phdm}), dark demethylation (k_{dem}), and Hg methylation (k_{met}) for each subbasin (colored markers) of the Mediterranean Sea (black lines), depth-integrated for surface water (0-100 m depth), intermediate water (100-600 m depth), and deep water (>600 m depth). The rate constants are computed by the model depending on environmental conditions (Table S2).

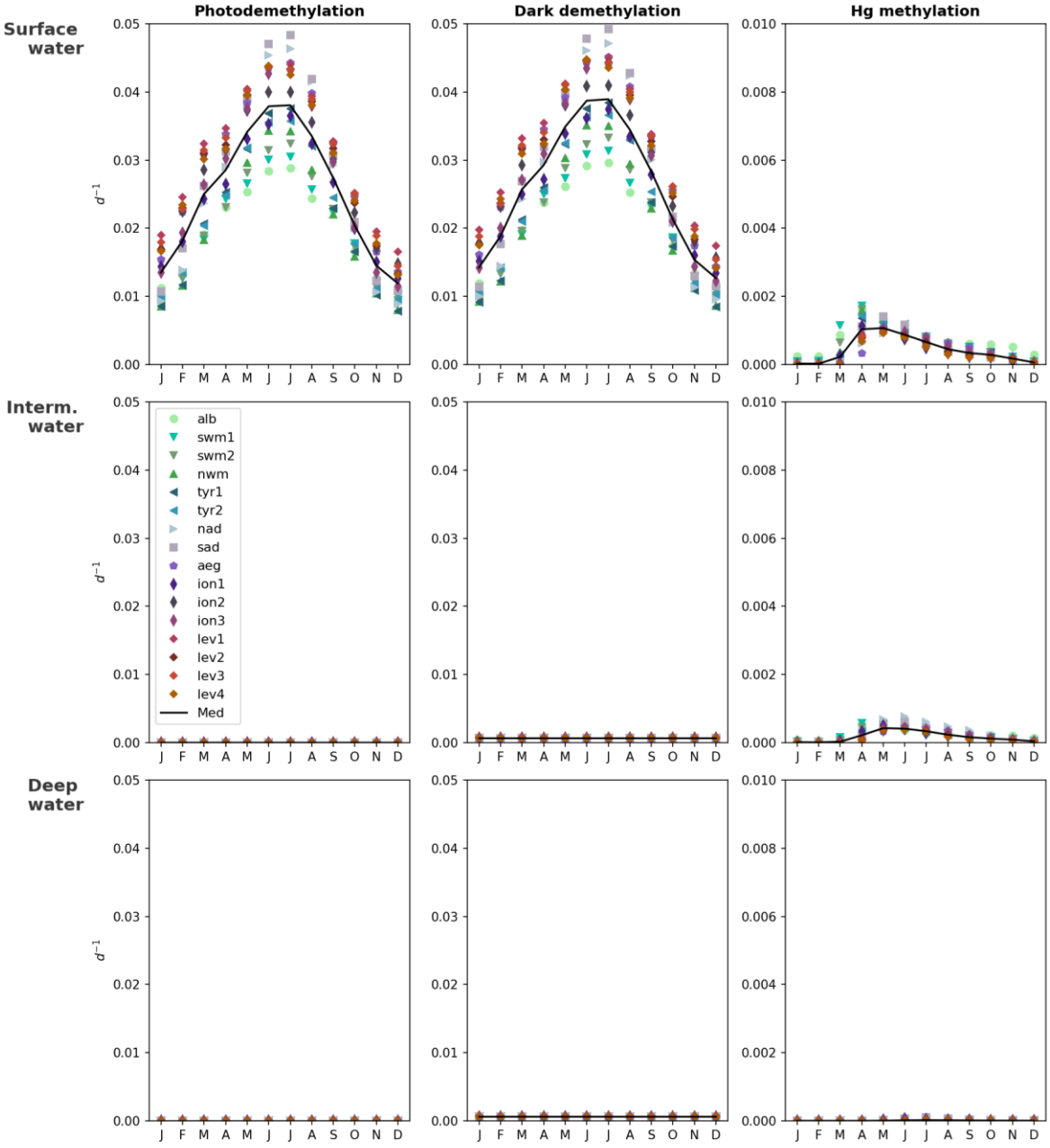

Figure S13. Spatial-temporal distribution of picophytoplankton biomasses on a carbon basis ($C_{phy,P3}$).

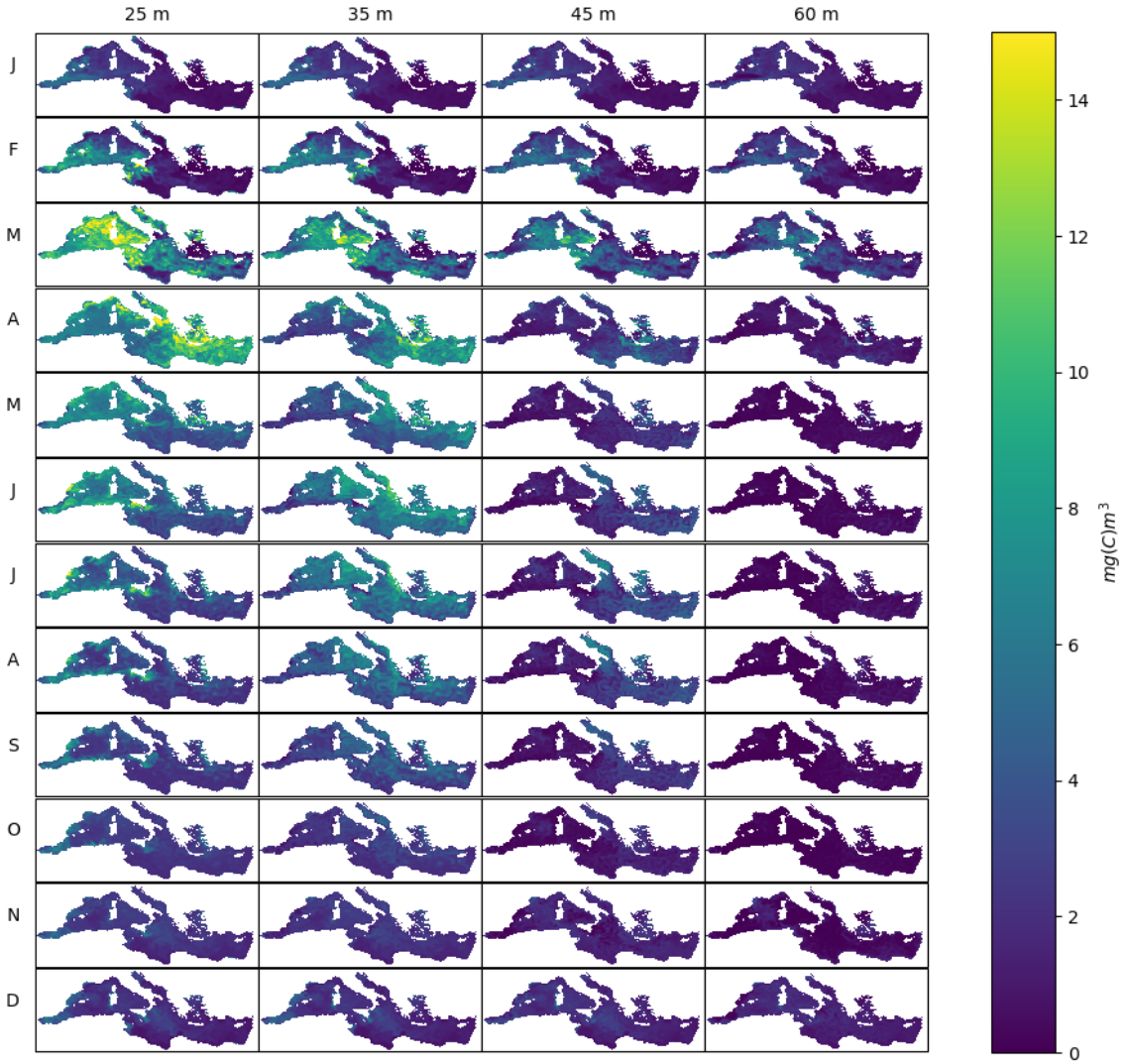

Figure S14. Spatial-temporal distribution of monomethylmercury (MMHg) concentrations in the surface water of the Mediterranean Sea.

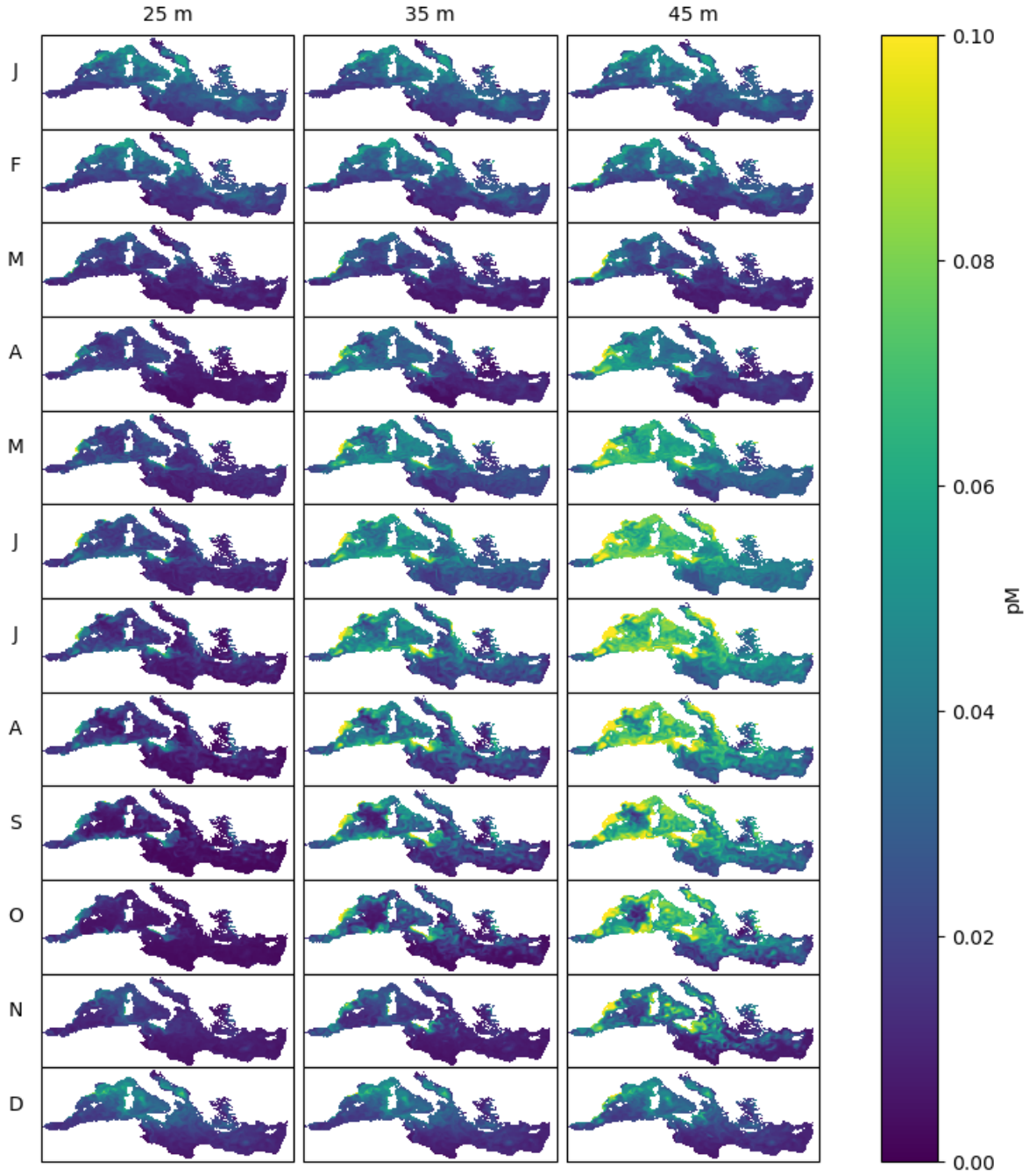

Figure S15. Spatial-temporal distribution of MMHg in picophytoplankton ($MMHg_{phy,P3}$).

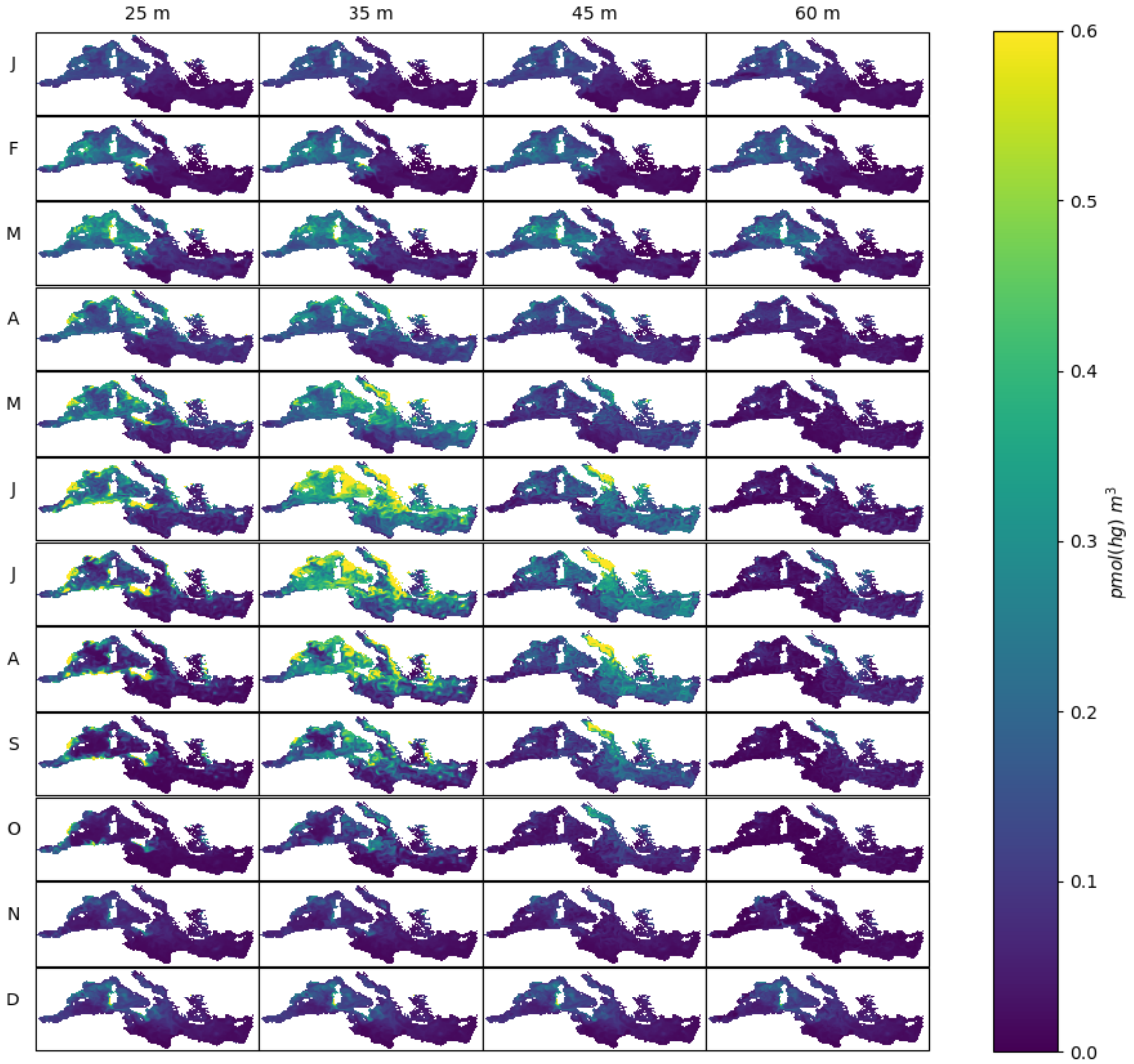

Figure S16. Spatial-temporal distribution of MMHg in autotrophic nanoflagellates ($MMHg_{phy,P2}$).

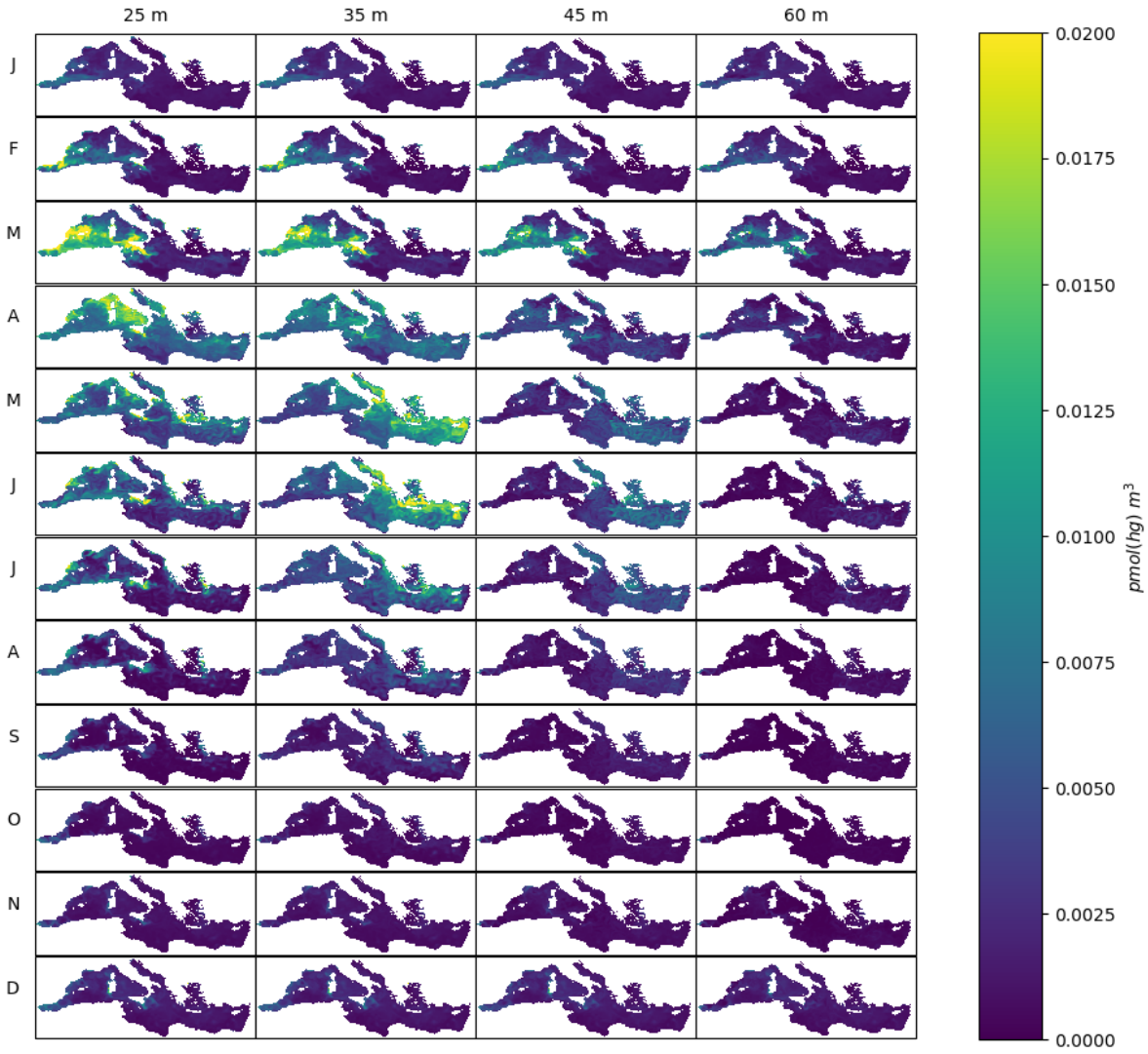

Figure S17. Spatial-temporal distribution of MMHg in diatoms ($MMHg_{phy,P1}$).

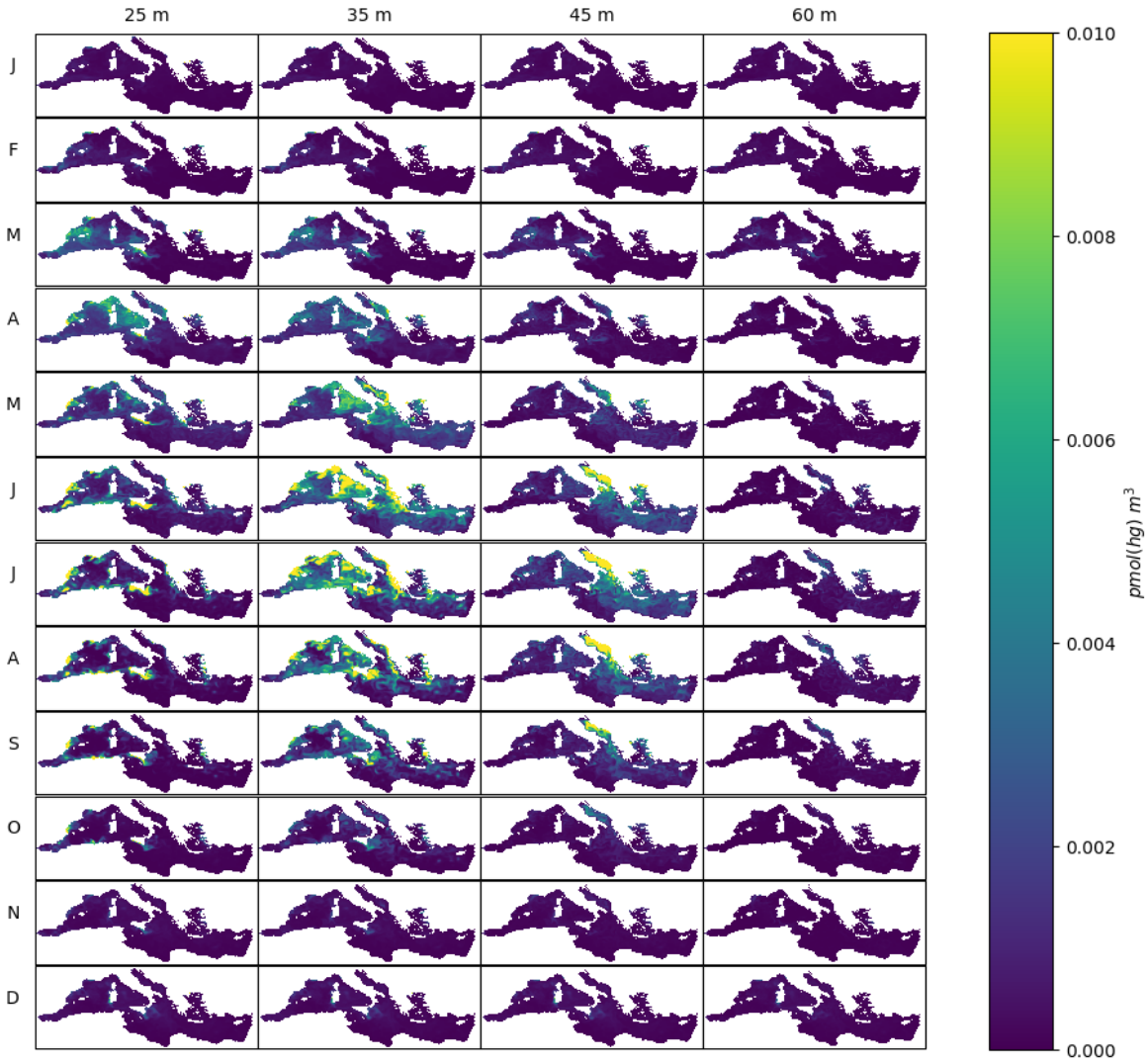

Figure S18. Spatial-temporal distribution of MMHg in large plankton ($MMHg_{phy,P4}$).

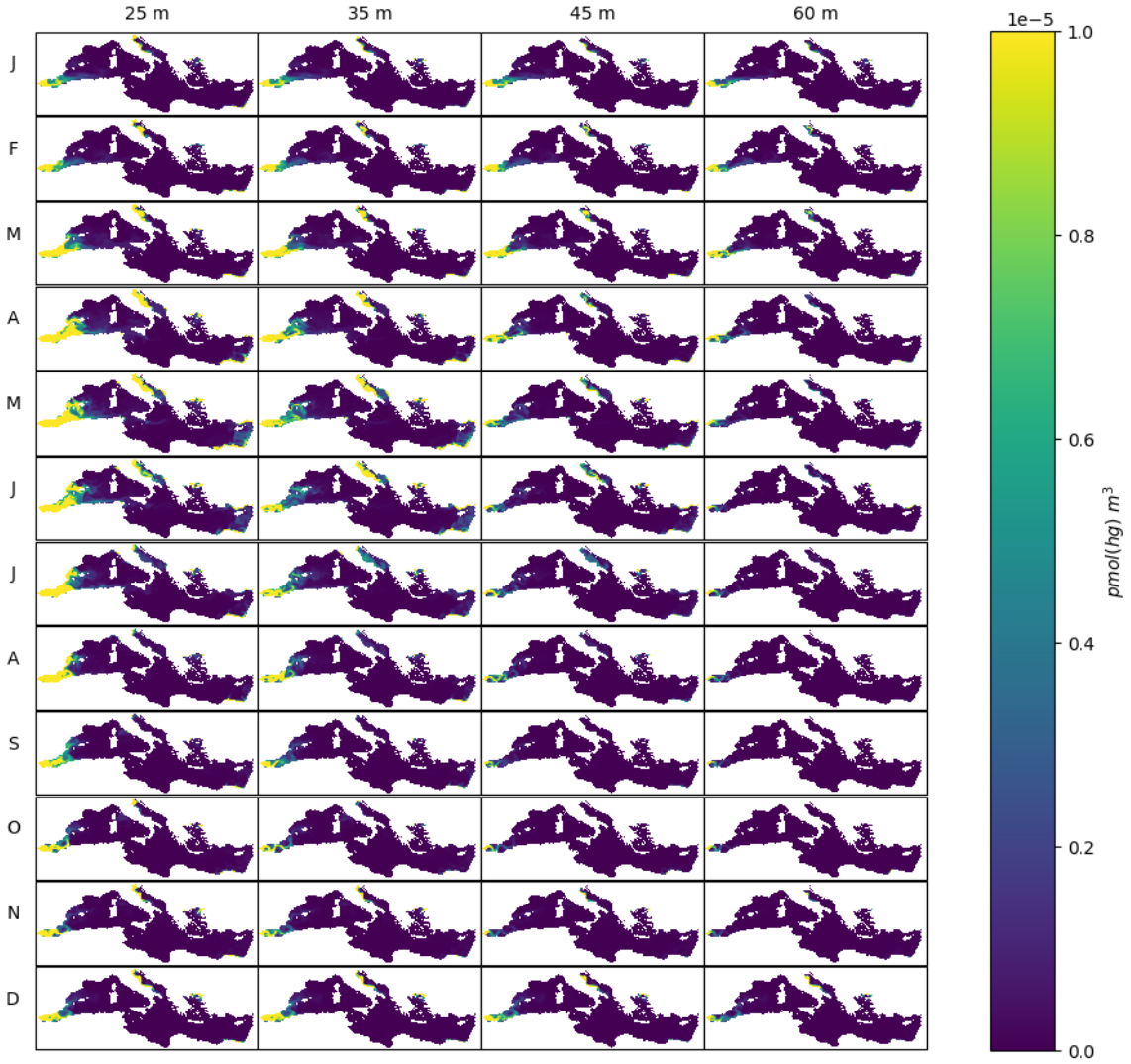

Figure S19. Spatial-temporal distribution of MMHg in heterotrophic nanoflagellates ($MMHg_{zoo,Z6}$).

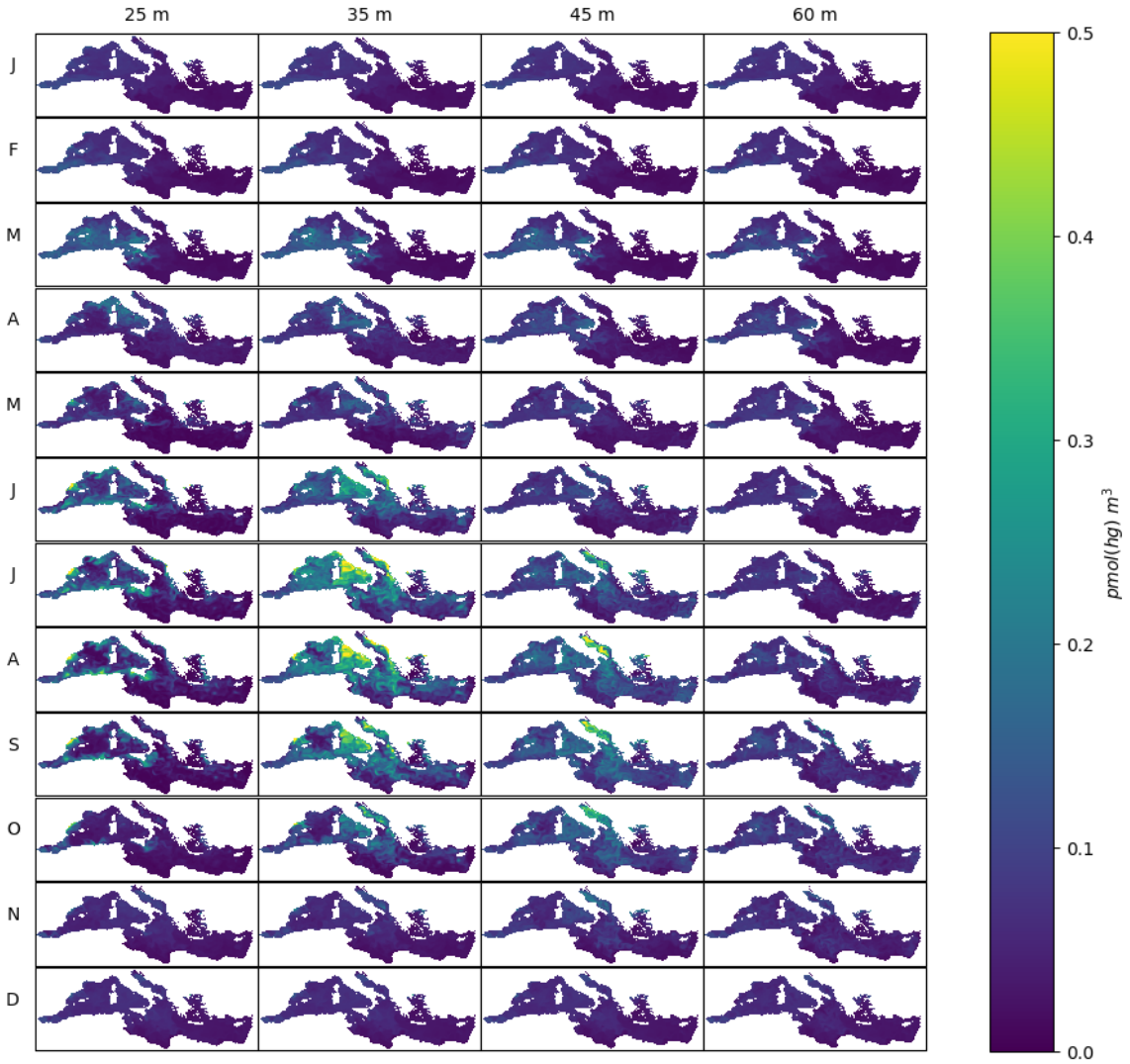

Figure S20. Spatial-temporal distribution of MMHg in microzooplankton ($MMHg_{zoo,Z5}$).

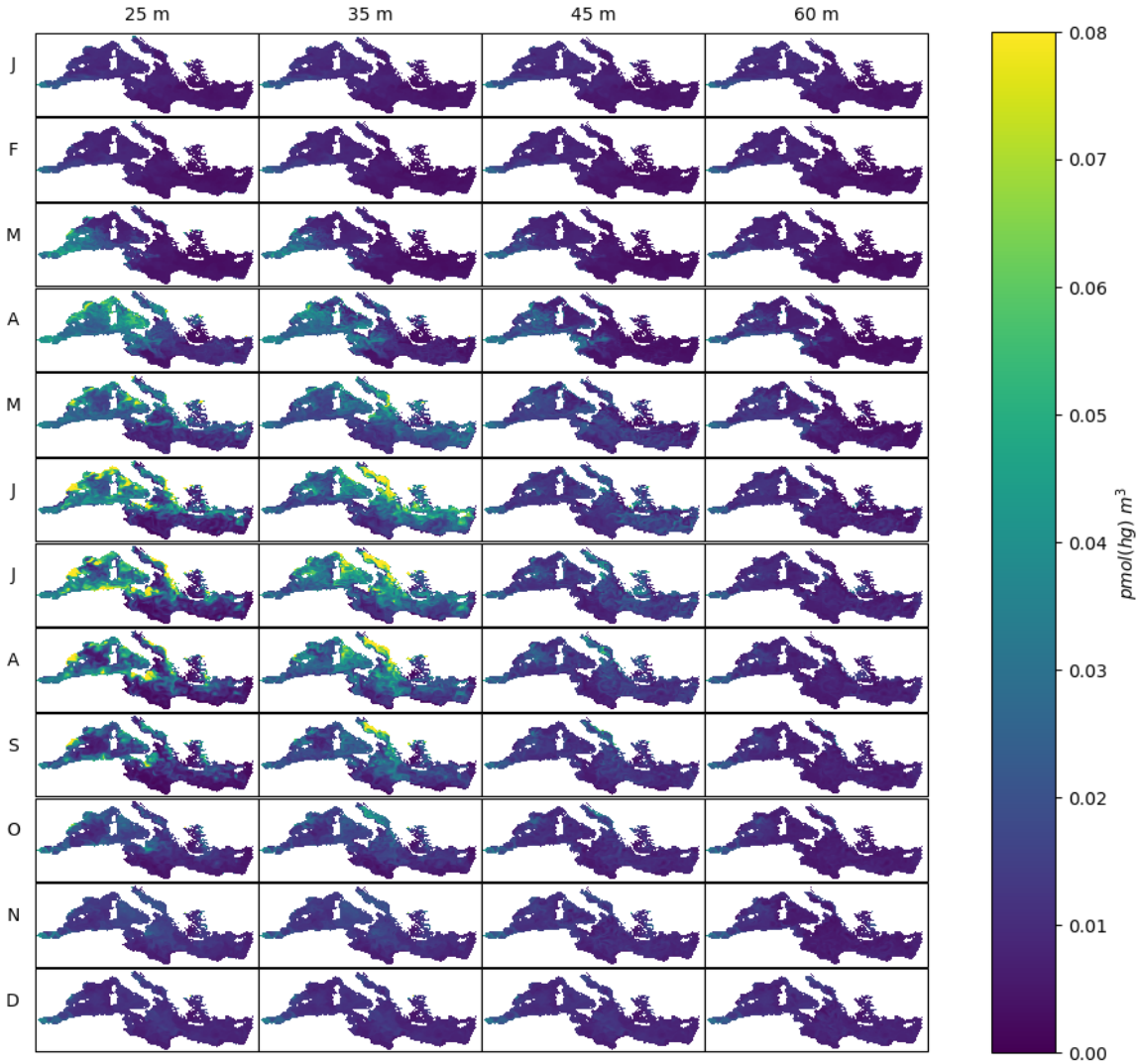

Figure S21. Spatial-temporal distribution of MMHg in large omnivorous zooplankton ($MMHg_{zoo,Z4}$).

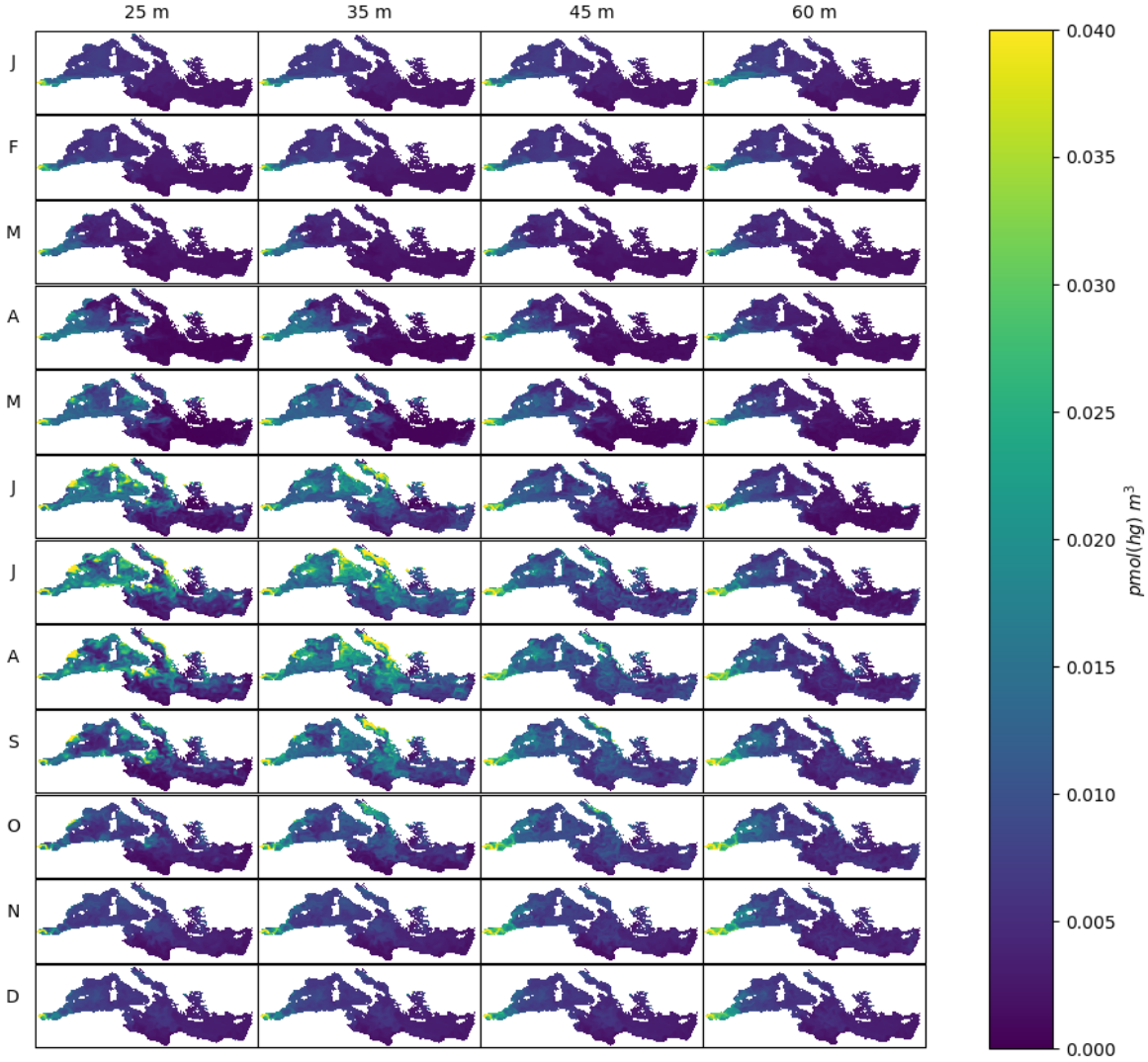

Figure S22. Spatial-temporal distribution of MMHg in large canivorous zooplankton ($MMHg_{zoo,Z3}$).

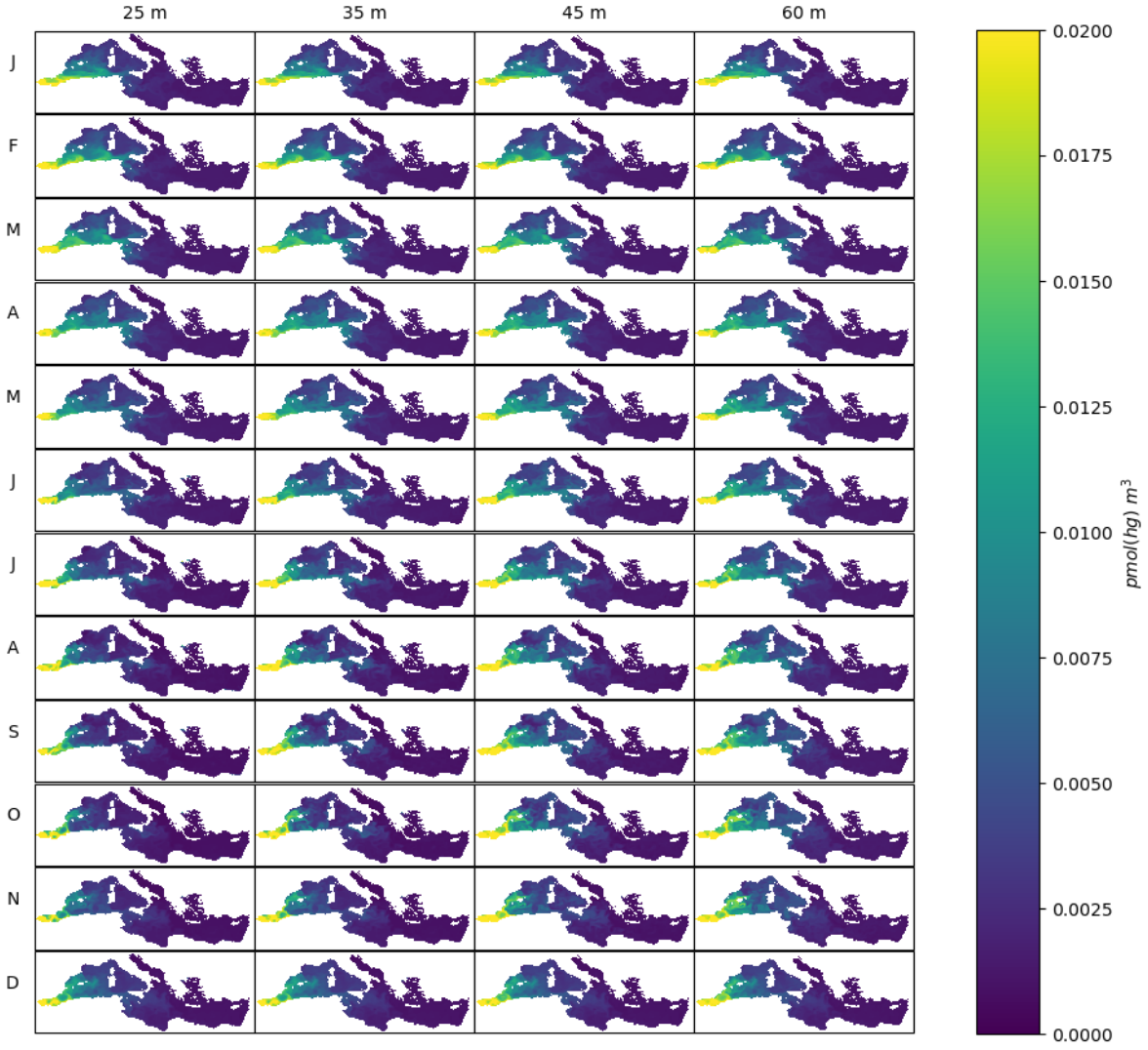

Figure S23. Spatial-temporal distribution of biomasses of heterotrophic nanoflagellates, on a carbon basis ($C_{zoo,Z6}$).

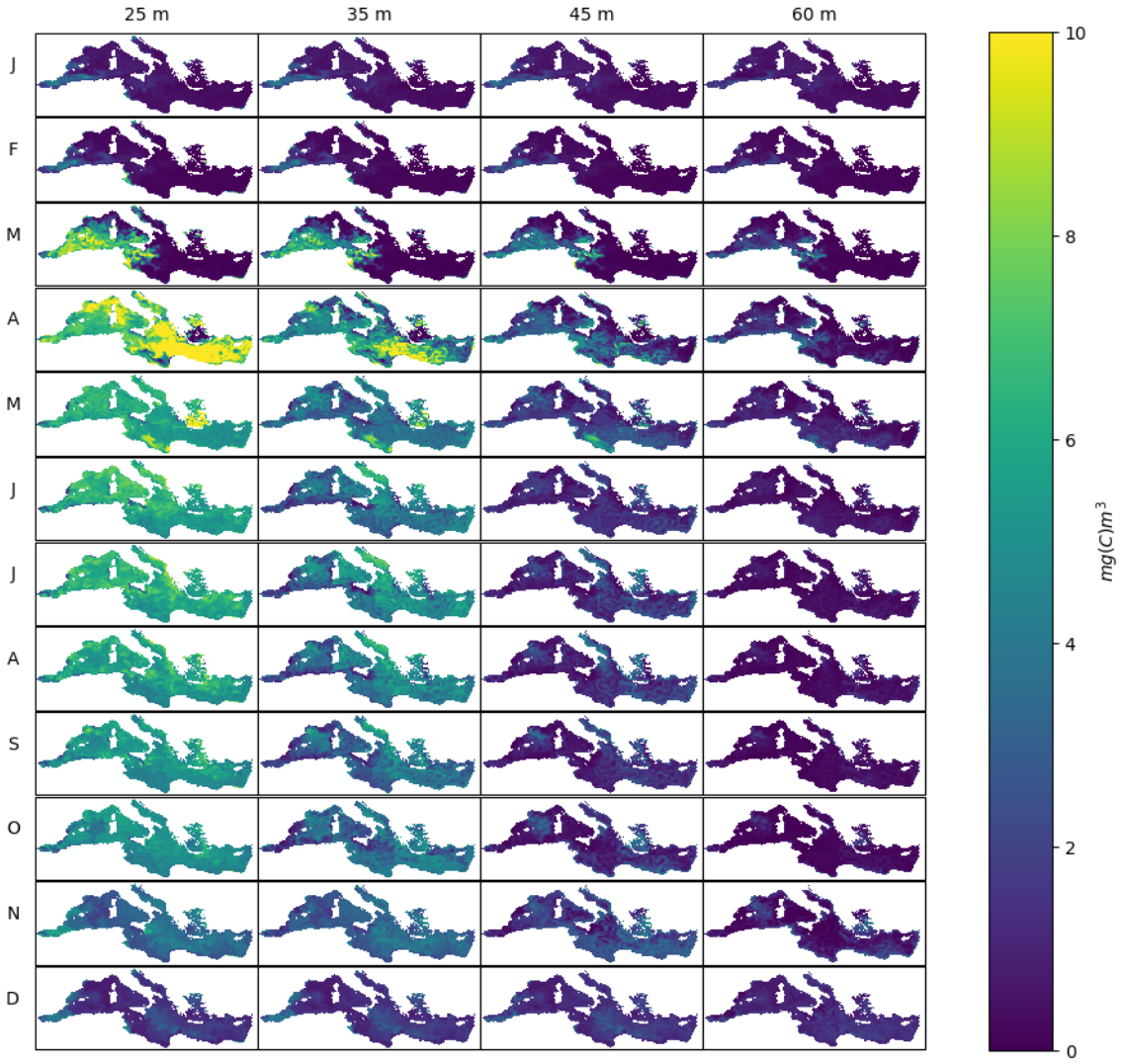

Figure S24. Spatial-temporal distribution of biomasses of carnivorous zooplankton, on a carbon basis ($C_{zoo,Z3}$).

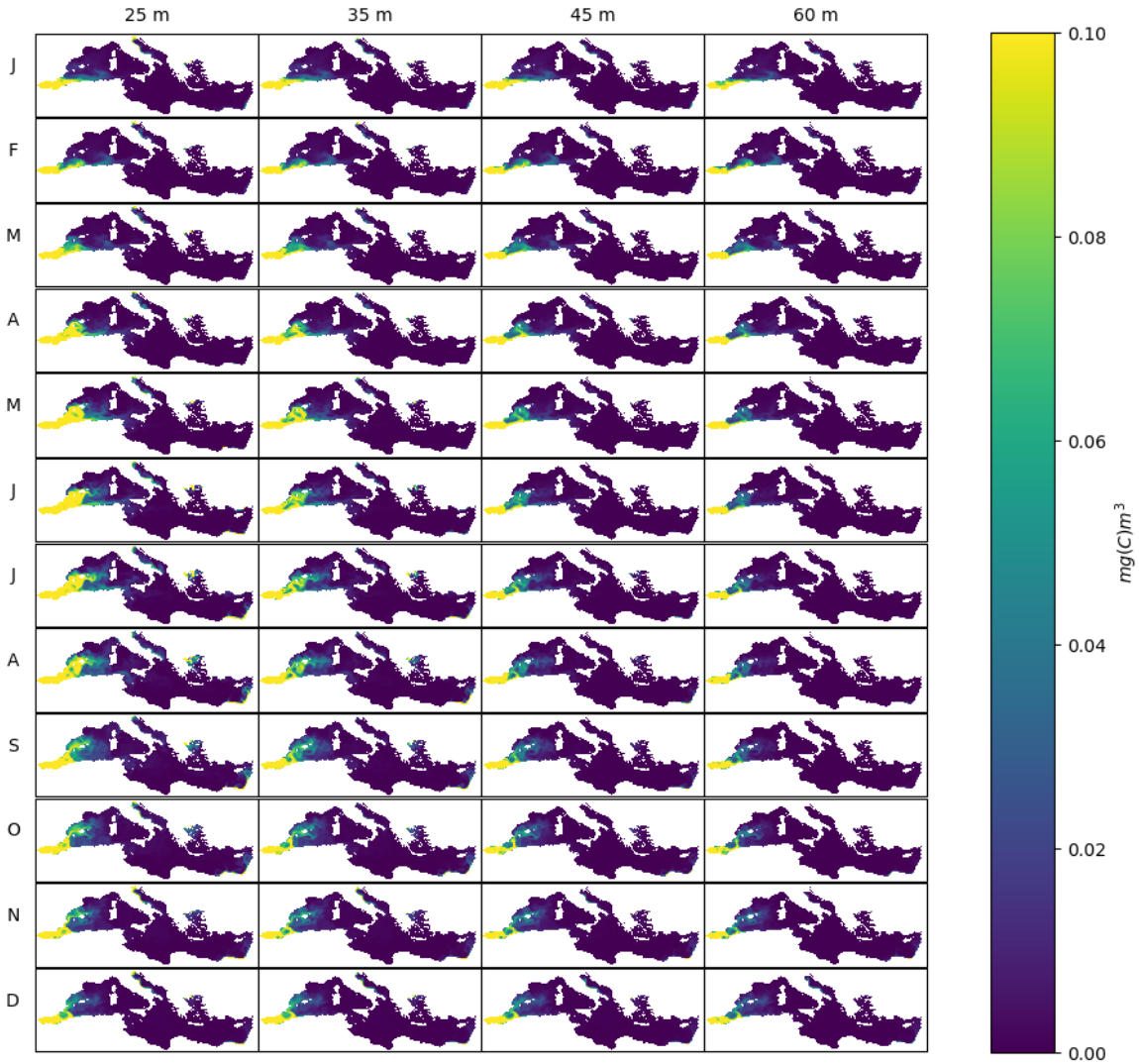

Ahmed, A.M.A., Purwanto, P., Sunoko, H.R., 2019. Consequences of Mercury Used by Artisanal and Small-Scale Gold Mining Processes a Case of River Nile State Sudan. J. Ecol. Eng. 20, 106–115.

Bourgeois, S., Pruski, A.M., Sun, M.Y., Buscail, R., Lantoine, F., Kerhervé, P., Vétion, G., Rivière, B., Charles, F., 2011. Distribution and lability of land-derived organic matter in the surface sediments of the Rhône prodelta and the adjacent shelf (Mediterranean Sea, France): A multi proxy study. Biogeosciences 8, 3107–3125. doi:10.5194/bg-8-3107-2011

Cossa, D., Averty, B., Pirrone, N., 2009. The origin of methylmercury in open Mediterranean waters. Limnol. Oceanogr. 54, 837–844. doi:10.4319/lo.2009.54.3.0837

Cossa, D., Durrieu de Madron, X., Schäfer, J., Guédron, S., Marusczak, N., Castelle, S., Naudin, J.J., 2018. Sources and exchanges of mercury in the waters of the Northwestern Mediterranean margin. Prog. Oceanogr. 163, 172–183. doi:10.1016/j.pocean.2017.05.002

Cossa, D., Durrieu de Madron, X., Schäfer, J., Lanceleur, L., Guédron, S., Buscail, R., Thomas, B., Castelle, S., Naudin, J.-J., 2017. The open sea as the main source of methylmercury in the water column of the Gulf of

Lions (Northwestern Mediterranean margin). Geochim. Cosmochim. Acta 199, 222–237. doi:10.1016/j.gca.2016.11.037

Cossa, D., Knoery, J., Bănaru, D., Harmelin-Vivien, M., Sonke, J.E., Hedgecock, I.M., Bravo, A.G., Rosati, G., Canu, D., Horvat, M., Sprovieri, F., Pirrone, N., Heimbürger-Boavida, L.-E., 2022. Mediterranean Mercury Assessment 2022: An Updated Budget, Health Consequences, and Research Perspectives. Environ. Sci. Technol. doi:10.1021/acs.est.1c03044

Heimbürger, L.-E., Cossa, D., Marty, J.-C., Migon, C., Averty, B., Dufour, A., Ras, J., 2010. Methylmercury distributions in relation to the presence of nano- and picophytoplankton in an oceanic water column (Ligurian Sea, North-western Mediterranean). Geochim. Cosmochim. Acta 74, 5549–5559. doi:10.1016/j.gca.2010.06.036

Hines, M.E., Horvat, M., Faganeli, J., Bonzongo, J.C.J., Barkay, T., Major, E.B., Scott, K.J., Bailey, E.A., Warwick, J.J., Lyons, W.B., 2000. Mercury biogeochemistry in the Idrija River, Slovenia, from above the mine into the Gulf of Trieste. Environ. Res. 83, 129–139. doi:10.1006/enrs.2000.4052

Jørgensen, S.E., Friis, M.B., Henriksen, J., Jørgensen, L.A., Mejer, H.F., 1979. Handbook of Envirnmental Data and Ecological Parameters. Pergamon Press, International Society for Ecological Modelling.

Palanques, A., Guillén, J., Puig, P., Grimalt, J.O., 2020. Effects of flushing flows on the transport of mercury-polluted particulate matter from the Flix Reservoir to the Ebro Estuary. J. Environ. Manage. 260. doi:10.1016/j.jenvman.2019.110028

Panagos, P., Jiskra, M., Borrelli, P., Liakos, L., Ballabio, C., 2021. Mercury in European topsoils: Anthropogenic sources, stocks and fluxes. Environ. Res. 201, 111556. doi:10.1016/j.envres.2021.111556

Ramondenc, S., Lombard, F., Santinelli, C., Stemmann, L., Gorsky, G., Guidi, L., 2016. An initial carbon export assessment in the Mediterranean Sea based on drifting sediment traps and the Underwater Vision Profiler data sets. Deep. Res. Part I 117, 107–119. doi:10.1016/j.dsr.2016.08.015

Vignati, D.A.L., Burdino, E., Congiu, A.M., Cicala, F., Pardos, M., Nieddu, G.F., Ugazio, G., 2008. Quality evaluation of sediments from 24 tributaries of the Po River, Italy. Water. Air. Soil Pollut. 190, 129–141. doi:10.1007/s11270-007-9586-7

Ward, B.A., Dutkiewicz, S., Jahn, O., Follows, M.J., 2012. A size-structured food-web model for the global ocean. Limnol. Oceanogr. 57, 1877–1891. doi:10.4319/lo.2012.57.6.1877

Zhang, Y., Jaeglé, L., Thompson, L., 2014. Natural biogeochemical cycle of mercury in a global three-dimensional ocean tracer model. Global Biogeochem. Cycles 28, 553–570. doi:10.1002/2014GB004814

Zhang, Y., Soerensen, A.L., Schartup, A.T., Sunderland, E.M., 2020. A global model for methylmercury formation and uptake at the base of marine food webs. Global Biogeochem. Cycles 34, 1–21. doi:10.1029/2019GB006348